# Model of Excitation-Contraction Coupling of Rat Neonatal Ventricular Myocytes

Topi Korhonen,[†] Sandra L. Hänninen,[†] and Pasi Tavi[‡*]
[†]Institute of Biomedicine, Department of Physiology and Biocenter Oulu, University of Oulu, Oulu, Finland; and [‡]Department of Biotechnology and Molecular Medicine, A. I. Virtanen Institute for Molecular Sciences, University of Kuopio, Kuopio, Finland

ABSTRACT The neonatal rat ventricular myocyte culture is one of the most popular experimental cardiac cell models. To our knowledge, the excitation-contraction coupling (ECC) of these cells, i.e., the process linking the electrical activity to the cytosolic $Ca^{2+}$ transient and contraction, has not been previously analyzed, nor has it been presented as a complete system in detail. Neonatal cardiomyocytes are in the postnatal developmental stage, and therefore, the features of their ECC differ vastly from those of adult ventricular myocytes. We present the first complete analysis of ECC in these cells by characterizing experimentally the action potential and calcium signaling and developing the first mathematical model of ECC in neonatal cardiomyocytes that we know of. We show that in comparison to adult cardiomyocytes, neonatal cardiomyocytes have long action potentials, heterogeneous cytosolic $Ca^{2+}$ signals, weaker sarcoplasmic reticulum $Ca^{2+}$ handling, and stronger sarcolemmal $Ca^{2+}$ handling, with a significant contribution by the $Na^+/Ca^{2+}$ exchanger. The developed model reproduces faithfully the ECC of rat neonatal cardiomyocytes with a novel description of spatial cytosolic $[Ca^{2+}]$ signals. Simulations also demonstrate how an increase in the cell size (hypertrophy) affects the ECC in neonatal cardiomyocytes. This model of ECC in developing cardiomyocytes provides a platform for developing future models of cardiomyocytes at different developmental stages.

## INTRODUCTION

Excitation-contraction coupling (ECC) forms the basis of cardiac function at the cellular level. The ECC process involves several nonlinear components that connect the electrical excitation at the cell membrane to the generation of cytosolic $Ca^{2+}$ signals triggering cell contraction (1). Due to the complexity of ECC, mathematical modeling has been used to facilitate understanding of the behavior and features of this system. At the present time, several mathematical models exist for ECC in myocytes from different species and different regions of the adult mammalian heart (2–8). In contrast, only a few models of action potential (AP) or ECC in developing cardiomyocytes have been developed (9,10).

Cardiomyocytes isolated from adult heart are terminally differentiated and do not divide or grow if cultured. However, if cardiomyocytes are isolated before differentiation is complete, e.g., just after birth, when they still have the ability to grow, divide, and differentiate, they can be used for long-term cell culture applications. Consequently, these primary cultures of rat neonatal ventricular cardiomyocytes are among the few cardiac cell culture models and are therefore widely used in biochemical, molecular biology and cellular signaling research (11,12). Neonatal cardiomyocytes are isolated for culture at the transitional period where the cells undergo dramatic changes from the phenotype of fetal myocytes to postnatal and adult myocytes (13). Culturing itself further shapes the phenotype of these neonatal cells (14,15). The neonatal cells have unique features. For example, they lack the T-tubule system (1,15) that plays a central role in the ECC of adult ventricular myocytes, and unlike their adult counterparts, they have the ability to maintain cytosolic $Ca^{2+}$ signaling without sarcoplasmic reticulum (SR) $Ca^{2+}$ release (1,16,17). The lack of T-tubules leads to more heterogeneous cytosolic $Ca^{2+}$ signals than in adult myocytes (1). From the mathematical modeling point of view, this requires a more complex description of cytosolic $[Ca^{2+}]$ ($[Ca^{2+}]_i$) in the neonatal model compared to the common-pool cytosol with one or a few additional compartments that is generally used in adult ventricular myocyte models (2,6,8). From a physiological point of view, this may attribute some unanticipated features to neonatal cells.

The purpose of this study was to 1), characterize the special features involved in the ECC of cultured rat neonatal ventricular myocytes; and 2), develop a mathematical model of the ECC in these cells that runs in a normal desktop PC but is complex enough to explain the important ECC features of these cells that distinguish them from other ventricular myocytes. In our experiments on neonatal myocytes, we quantified the AP, the SR $Ca^{2+}$ storage capacity, and the cytosolic $Ca^{2+}$ signaling with the contributions of sarcolemmal (SL) and SR $Ca^{2+}$ fluxes. Based on our experimental AP and $Ca^{2+}$ signaling data, as well as data from other studies with rat neonatal myocytes in the literature, we developed and validated a mathematical model that faithfully reproduces the ECC of rat neonatal myocytes. This model is unique in that it includes cytosolic $Ca^{2+}$ as a function of time and spatial coordinates. A similar approach has been used in models of cytosolic $Ca^{2+}$ diffusion in atrial cardiomyocytes (18) and rabbit neonatal cardiomyocytes (19),

*Submitted January 31, 2008, and accepted for publication October 27, 2008.*

*Correspondence: pasi.tavi@oulu.fi

Editor: David A. Eisner.



0006-3495/09/02/1189/21 $2.00

doi: 10.1016/j.bpj.2008.10.026

but never in conjunction with both AP-generating SL ion currents and components of SR $Ca^{2+}$ dynamics.

Here, using experiments and modeling, we present the first complete analysis of ECC in cultured rat neonatal ventricular cardiomyocytes and propose a novel mathematical model to be used as a tool to study ECC function in these cells. With the simulations, we show that the largest differences between adult and neonatal cells are in AP length and how $Ca^{2+}$ signals are generated and regulated from SL and SR sources during the AP. The simulations also show how the ECC of a neonatal cardiomyocyte during hypertrophy is likely to be shaped by the increase in cytosol volume.

## MATERIALS AND METHODS

### Cell isolation and culturing

The isolation and culturing of neonatal rat ventricular cardiomyocytes was performed as previously described (11,12). Briefly, neonatal rat cardiomyocytes were isolated 1–2 days after birth. Ventricles were excised, cut into small pieces, and incubated for 1 h in a solution containing 100 mM NaCl, 10 mM KCl, 1.2 mM $KH_2PO_4$, 4.0 mM $MgSO_4$, 50 mM taurine, 20 mM glucose, 10 mM HEPES, 2 mg/ml collagenase type II (Worthington, Lakewood, NJ), 2 mg/ml pancreatin (P-3292, Sigma, St. Louis, MO) and 1% penicillin-streptomycin. After incubation, the detached cells were collected in 15-ml Falcon tubes and centrifuged for 5 min at 160 *g*. The supernatant and the top layer of the pellet containing damaged cells were discarded and the isolated cardiomyocytes were plated on 35-mm fibronectin-coated plastic dishes. The cells were cultured to reach confluence in Dulbecco's modified Eagle's medium (DMEM) containing 10% FBS and 1% penicillin-streptomycin. The experiments were performed after 4–5 days of culturing.

### Electrophysiology and $Ca^{2+}$ imaging

For AP recording and $Ca^{2+}$ imaging, the culturing dishes were placed in a custom-made perfusion system built into an Olympus Fluoview 1000 confocal inverted microscope. Cells were held at a steady 32–35°C by continuous superfusion with preheated DMEM + Glutamax I (Gibco, Carlsbad, CA) culturing medium (pH 7.4, bubbled with 95% $O_2$/5% $CO_2$). For $Ca^{2+}$ imaging, cells were loaded in DMEM + 1 mM probenecid solution for 1 h at 37°C in incubator with Fluo-4-AM-ester or Fluo-3-AM-ester (10 $\mu$M, dissolved in pluronic DMSO, Molecular Probes, Eugene, OR). The solution was changed two times and cells were incubated at room temperature (20–22°C) at least 30 min for the dye to de-esterify.

To measure myocyte calcium signals, Fluo-loaded myocytes were excited at 488 nm and the emitted light was collected with a spectral detector from 520 to 620 nm through a 20× or 60× objective lens. To excite the cells, myocytes were stimulated with 1-ms voltage pulses at 50% over the excitation threshold through two platinum wires located one on each side of the petri dish. At the time of electrical stimulation or spontaneous activity, cells were line-scanned at 400–600 Hz, depending on the length of the scanning line, with a fixed pixel time of 10 $\mu$s with the 20× objective and 2 $\mu$s with the 60× objective. Fluo- fluorescence intensity is expressed as an $F/F_0$ ratio, where $F$ is the background-subtracted fluorescence intensity and $F_0$ is the background-subtracted minimum fluorescence value measured from each cell at rest.

To record action potentials, the whole-cell patch-clamp method in current-clamp mode was used. Electrode resistances were 10–15 MΩ and the pipette solution was (in mM) 130 KCl, 5 $Na_2$-phosphocreatine, 5 Mg-ATP, 1 EGTA, and 10 HEPES (pH adjusted to 7.2 with KOH). APs were filtered at 2 kHz and acquired at 10 kHz. Clampex 9.2 software, an Axopatch-1D amplifier, and Digidata 1322A A/D-D/A (Axon Instruments, Union City, CA) were used for data acquisition.

### Mathematical modeling

A model of cultured rat neonatal ventricular cardiomyocytes was developed. The purpose of the modeling was to define the fundamental components needed to reproduce the intracellular $Ca^{2+}$ signaling and AP features observed in the experiments. The model includes SR and SL membranes with ion channels and an SR $Ca^{2+}$ store. Intracellular $Ca^{2+}$ signals and diffusion of the $[Ca^{2+}]_i$ was modeled as a function of a space coordinate in addition to a time coordinate. For a complete list of model equations and parameters, see the Appendix and Tables 2–5. The model parameters were estimated, whenever possible, based on experimental data. The data used were from rat neonatal cardiomyocytes cultured for 3–5 days, or, when necessary, very similar cells. The parameters were estimated by direct fitting (e.g., for inactivation and activation of ion current) or indirect fitting (e.g., for amount of SERCA based on the decay of $Ca^{2+}$ transient). In either case, the fit was considered satisfactory when the values and the curves of the fits were within the standard error of the mean experimental values.

### Structure of the model

The model cell was assumed to have a spherical shape. As in real cells, the nucleus was located at the center of the cell, surrounded by a thin layer-like compartment representing the SR (Fig. 1). The radius from the center of the cell to the surface of the SR ($r_{SR}$) was set to 6 $\mu$m according to our measurements of the diameters of the nucleus + SR in the center of neonatal cardiomyocytes (6.0 ± 0.2 $\mu$m, $n = 25$). The distance between the $r_{SR}$ and $r_{nucleus}$ determines the volume of the SR (Fig. 1). Based on the fitting of the SR volume (see Sarcoplasmic reticulum in Methods), $r_{nucleus}$ was set to 5.7934 $\mu$m. The distance between the SR and SL is 4.5 $\mu$m based on our cytosolic $Ca^{2+}$ diffusion recordings (see Results). The radius of the cell ($r_{SL}$) is thus 10.5 $\mu$m, which reproduces the cell membrane capacitance of 13.9 pF, comparable to experimental results (13.8 ± 1.3 pA/pF (20); ~15 pA/pF in cells cultured for 3 days (14)).

### Sarcolemmal ion channels

#### *L- and T-type $Ca^{2+}$ currents*

Both L- and T-Type $Ca^{2+}$ channels ($I_{CaL}$ and $I_{CaT}$, respectively) are functionally expressed in cultured neonatal ventricular rat cardiomyocytes (14,21), providing a voltage-activated $Ca^{2+}$ intrusion to the cell. The model of $I_{CaL}$ is described by the equation

$$I_{CaL} = G_{CaL} d f f_{Ca} 4 \frac{VF^2}{RT} \frac{\left[Ca^{2+}\right]_{subSL} e^{2VF/RT} - 0.341\left[Ca^{2+}\right]_o}{e^{2VF/RT} - 1}, \quad (1)$$

which is adapted from the model of Tusscher et al. (5). The model has one voltage-dependent activation gate ($d$) and two inactivation gates for voltage-dependent inactivation ($f$) and for $[Ca^{2+}]_i$-dependent inactivation ($f_{Ca}$). The steady-state curves for the voltage-dependent gates ($d$ and $f$) were set to those recorded from 3-day-cultured ventricular neonatal rat cardiomyocytes (21). The time-constant curve of $f$ was scaled to correspond to the experimental value for slow $Ca^{2+}$-independent inactivation (21). The $Ca^{2+}$-dependent inactivation is rapid (1), and thus, the time constant for $f_{Ca}$ was set to the same as the fast component of the experimental $I_{CaL}$ inactivation (21).

Our model simulates the spatial $Ca^{2+}$ gradients within the cytosol and the $Ca^{2+}$-dependent inactivation of $I_{CaL}$ was set to depend on the subsarcolemmal $[Ca^{2+}]$ ($[Ca^{2+}]_{subSL}$). The $Ca^{2+}$-dependent inactivation of the $I_{CaL}$ model was originally formulated to depend on the total cytosolic $[Ca^{2+}]_i$ in the common-pool cytosol (5). The $[Ca^{2+}]_{subSL}$ increases to higher values

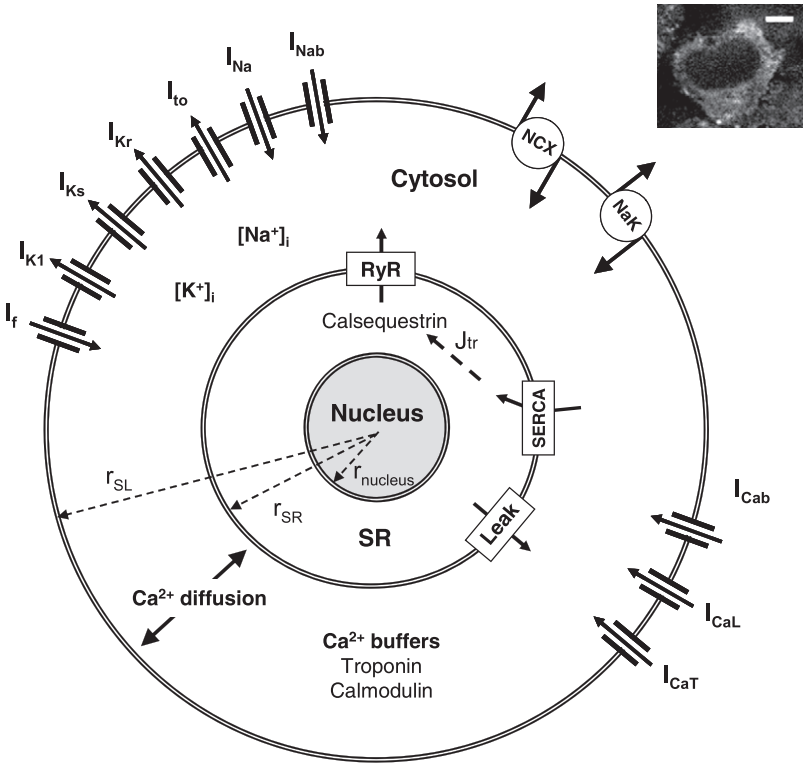


FIGURE 1 Schematic diagram of the spherically shaped model of a cultured rat neonatal ventricular cardiomyocyte (the radii $r_{SL}$, $r_{SR}$, and $r_{nucleus}$ are not to scale). The SL ion currents are the hyperpolarization-activated current ($I_f$), the time-independent $K^+$ current ($I_{K1}$), the slow and rapid delayed rectifier $K^+$ currents ($I_{Ks}$ and $I_{Kr}$), the transient outward $K^+$ current ($I_{to}$), the fast $Na^+$ current ($I_{Na}$), the background $Na^+$ current ($I_{Nab}$), the $Na^+/Ca^{2+}$ exchanger (NCX), the $Na^+/K^+$-ATPase (NaK), the background $Ca^{2+}$ current ($I_{Cab}$) and the L- and T-type $Ca^{2+}$ currents ($I_{CaL}$ and $I_{CaT}$). The $Ca^{2+}$ diffuses radially and is buffered by troponin and calmodulin in the cytosol. The SR is located on the surface of the nucleus. The SR is divided into uptake and release compartments ($SR_{uptake}$ and $SR_{release}$, respectively, not shown in figure). The $Ca^{2+}$ is transported between these compartments by diffusion ($J_{tr}$). $Ca^{2+}$ fluxes between $SR_{uptake}$ and cytosol are passive diffusion (leak) and $Ca^{2+}$ uptake by SERCA. In the $SR_{release}$ compartment, $Ca^{2+}$ is buffered by calsequestrin. $Ca^{2+}$ is released from $SR_{release}$ to the cytosol via ryanodine receptors (RyR). The inset shows a real cultured rat neonatal ventricular cell loaded with Fluo-4 $Ca^{2+}$ indicator in a confocal microscope (scale bar, 5 $\mu$m). The nucleus (black area in the center) and the surrounding cytosol with Fluo-4 signal can be seen.

more quickly than the total cytosolic $[Ca^{2+}]_i$, and thus, we adjusted the original steady-state curve of the $Ca^{2+}$-dependent inactivation (5) to higher $[Ca^{2+}]$ values (Fig. 2 *A*).

The maximum conductance for $I_{CaL}$ ($G_{CaL}$) was fitted to reproduce the SL-originated cytosolic $[Ca^{2+}]$ signals observed in our experiments (see Results). In the voltage-clamp simulation, the fitted conductance produced an I/V relation and peak current of −5.9 pA/pF, which are in line with the I/V relations and peak currents measured from 3- to 5-day-cultured rat neonatal ventricular cardiomyocytes (−5.3 ± 0.5 pA/pF (21) and −6.6 ± 0.5 pA/pF (22); Fig. 2 *B*).

The model of the T-type $Ca^{2+}$ channel is described by the equation

$$I_{CaT} = G_{CaT} bg(V - E_{Ca} + 106.5), \quad (2)$$

which is adapted from the model by Dokos et al. (4). The steady-state curves for activation ($b$) and inactivation ($g$), the maximum conductance ($G_{CaT}$), and the reversal potential of the current were fitted to the data from 2- to 3-day-cultured cardiomyocytes (14) (Fig. 2 *B*).

### *$Na^+/Ca^{2+}$ exchanger*

The model of the $Na^+/Ca^{2+}$ exchanger (NCX) was taken from the adult rat ventricular myocyte model of Pandit et al. (6). Fitting of the magnitude of $I_{NCX}$ was based on its effects on the decay of the $Ca^{2+}$ transient, resting potential (RP) and the duration of the AP.

### *Background currents*

Background $Na^+$ and $Ca^{2+}$ leak currents ($I_{Nab}$ and $I_{Cab}$) were modeled as linear ohmic currents. These currents represent the leak of these ions through the SL via nonspecific routes. The magnitudes were set to reproduce physiologically relevant diastolic concentrations and correct RP.

### *$Na^+/K^+$ ATPase*

The model of NaK ATPase was taken from the Luo and Rudy model (7) and fitted to maintain physiologically correct intracellular $Na^+$ and $K^+$ concentrations.

### *Fast $Na^+$ current*

The model of the fast $Na^+$ current ($I_{Na}$) is from the Pandit et al. model (6). The maximum conductance of the current was fitted to reproduce AP amplitude comparable to our experimental data.

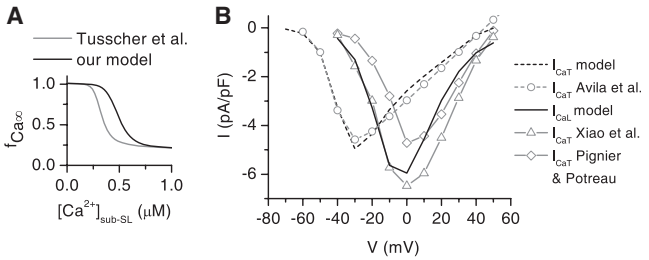


FIGURE 2 Properties of voltage-activated $Ca^{2+}$ currents of the model. (*A*) The steady-state curve for the $Ca^{2+}$-dependent inactivation gate of the $I_{CaL}$ model versus the cytosolic $Ca^{2+}$ concentration below SL (sub-SL) in our model (*black*) and in the model of Tusscher et al. (*gray*) (5). (*B*) The I/V relations of $I_{CaT}$ and $I_{CaL}$. The simulated I/V relation of $I_{CaT}$ (*black dashed line*) is compared to the I/V relation recorded by Avila et al. (14) (*gray circles with dashed line*). The simulated I/V relation of $I_{CaL}$ (*black solid line*) is compared to the I/V relations recorded by Xiao et al. (*gray triangles with solid line*) (22) and Pignier and Potreau (*gray diamonds with solid line*) (21). The I/V relation of Xiao et al. is constructed from their peak current in neonatal cells and the normalized I/V relation for adult myocytes, which is, according to Xiao et al., the same for neonatal cells (22). The $I_{CaT}$ was simulated as an individual ion channel model with the environmental conditions of Avila et al. (14). The simulated $I_{CaL}$ was taken from the voltage-clamp simulation of the whole myocyte model to provide a realistic sub-SL $[Ca^{2+}]_i$ contribution to the $Ca^{2+}$-dependent inactivation of the $I_{CaL}$, as is the case in the experimental whole-cell voltage-clamp data. The error bars of the experimental data were left out to clarify the figure.

### *Hyperpolarization-activated current*

The model of the hyperpolarization-activated current ($I_f$) carried by $Na^+$ (20%) and $K^+$ (80%) is described by the equation

$$I_f = G_f y[0.2(V - E_{Na}) + 0.8(V - E_K)], \quad (3)$$

which is adapted from the Pandit et al. model (6). The steady-state and time-constant curves for the gate $y$ (Fig. 3 *A*) were estimated from Fig. 2 *C* of Shi et al. (23). This reproduces the $I_f$ current with an approximately −70 mV activation threshold (Fig. 3 *A*), in line with the experimental data (24). The maximum conductance ($G_f$) was fitted to reproduce the current density of −0.71 ± 0.23 pA/pF at −95 mV (24) (Fig. 3 *A*). The data in these two studies (23,24) were recorded from 5- to 7-day-cultured rat neonatal ventricular cardiomyocytes.

### *Time-independent $K^+$ current*

The model of the time-independent $K^+$ current ($I_{K1}$) is described by the equation

$$I_{K1} = 0.0515\frac{[K^+]_o}{[K^+]_o + 210}\frac{V - E_K - 6.1373}{0.1653 + e^{0.0319(V - E_K - 6.1373)}}, \quad (4)$$

which is adapted from the Bondarenko et al. model (2). The model was fitted to data measured from freshly isolated rat neonatal ventricular cardiomyocytes (25). This is justified since the $I_{K1}$ does not change during 0–3 days of culturing (25). We fitted the $I_{K1}$ model to the average of the measured peak and steady-state currents, because the $I_{K1}$ model does not distinguish between these current types. This was considered reasonable as the difference between the peak and steady-state values is zero at membrane voltage ($V_m$) values above −90 mV and small at $V_m$ values below −90 mV (Fig. 3 *B*).

### *Transient outward $K^+$ current*

The model of the transient outward current ($I_{to}$) is from the Pandit et al. model (6). The model is described by the equation

$$I_{to} = G_{to} r(0.706s + 0.294s_{slow})(V - E_K), \quad (5)$$

where $r$ is the activation gate and $s$ and $s_{slow}$ are the fast and slow inactivation components. The steady-state curves for the activation and inactivation gates were fitted to data from 3- to 4-day-cultured myocytes (26) (Fig. 3 *C*). The time-constant curves of the inactivation time constants and the fractions for fast and slow inactivation were scaled to compare values measured at +30 mV from 5-day-cultured myocytes (27). The maximum conductance was fitted to reproduce an I/V relation comparable to the experimental recordings from 3- and 5-day-cultured myocytes (27,28) (Fig. 3 *C*).

### *Slow and rapid delayed rectifier $K^+$ currents*

The slow and rapid delayed rectifier $K^+$ currents ($I_{Ks}$ and $I_{Kr}$) are present in rat neonatal ventricular myocytes (20,29). For modeling the $I_{Ks}$ we used the Bondarenko et al. model (2) with a reduced activation time constant (based on the experimental $I_{Ks}$ traces (29)). For modeling the $I_{Kr}$, we used the Wang et al. model (30) with the previously described reversal potential modification (2). The approximate magnitudes of $I_{Ks}$ and $I_{Kr}$ were fitted to the experimental values (20,29). As previously (5), due to the difficulties in recording $I_{Kr}$ and $I_{Ks}$ magnitudes accurately with the whole-cell voltage clamp (20,31), the final fitting of the magnitudes of these currents was based on their effect on the AP repolarization.

## Sarcoplasmic reticulum

The SR was modeled to consist of two compartments, the release and the uptake compartments ($SR_{release}$ and $SR_{uptake}$, respectively). The time taken by the diffusion from $SR_{uptake}$ to $SR_{release}$ provides a realistic delay for the uptaken $Ca^{2+}$ to be available for the release again. The release compartment was assumed to be 10% of the total SR volume.

The $Ca^{2+}$ flux between the $SR_{uptake}$ and cytosol is described by the Shannon et al. model for the SR $Ca^{2+}$ ATPase (SERCA) and SR $Ca^{2+}$ leak (32). The model of SERCA was fitted according to our $Ca^{2+}$ transient decay measurements. In 4-day-cultured rat neonatal cardiomyocytes, the calsequestrin $Ca^{2+}$ buffer is expressed in the SR (33). We assume that the calsequestrin is located near the ryanodine receptors (RyRs), as in adult cardiomyocytes (1). The $Ca^{2+}$ is released from the $SR_{release}$ via RyR, which is described by the model of Sobie et al. (34) with two modifications. 1), In our model, the RyR represents the average behavior of all RyR molecules. The "coupling" factors used by Sobie et al. to model an RyR cluster constructed from several individual RyR models were thus removed. 2) The

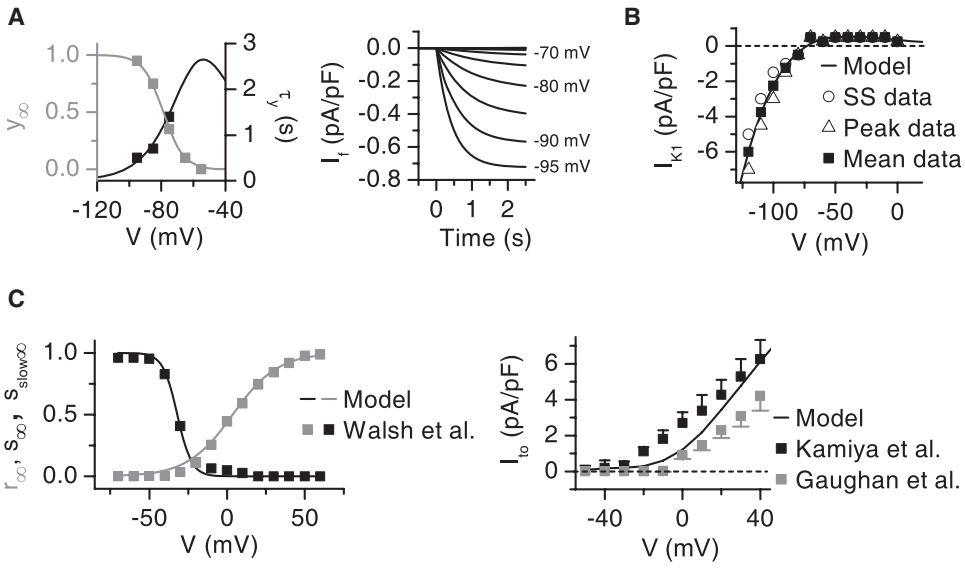


FIGURE 3 Properties of the pacemaker current ($I_f$) and repolarizing potassium currents. (*A*, *left*) The voltage-dependent steady-state curve (*gray*) and the activation time constant (*black*) of $I_f$ in the model (*solid lines*) and in the experimental data of Shi et al. (*squares*) (23). (*A*, *right*) The simulated $I_f$ current in the voltage-clamp experiment from a holding potential of −50 mV. At the time point of 0 s, voltage clamps were applied in the range of −55 mV to −95 mV with 5-mV intervals. Corresponding clamp voltages are shown with the current traces. The model of $I_f$ was simulated in the conditions of Robinson et al. (24). (*B*) The I/V relation of the model of $I_{K1}$ (*solid line*) compared to steady-state (SS), peak, and average of SS and peak current (*symbols*) measured by Wahler (25). The model of $I_{K1}$ was simulated in the environmental conditions of Wahler (25). (*C*, *left*) The voltage-dependent steady-state activation ($r_\infty$, *gray*) and slow and fast ($s_\infty$, $s_{slow\infty}$, *black*) inactivation curves in the model (*solid lines*) and as recorded by Walsh et al. (*squares*) (26). (*C*, *right*) Simulated I/V relation of the peak $I_{to}$ current (*solid line*) compared to those recorded by Kamiya et al. (*black squares*) (27) and Gaughan et al. (*gray squares*) (28).

model of Sobie et al. includes regulation of the RyR openings by the cytosolic $Ca^{2+}$ concentration near the SR ($[Ca^{2+}]_{subSR}$) and the $[Ca^{2+}]_{SR\text{-}release}$. The linear dependence of the $K_m$ for $[Ca^{2+}]_{subSR}$ from $[Ca^{2+}]_{SR\text{-}release}$ was replaced with sigmoidal dependence (Appendix, Eq. 88). We consider it more realistic that the $K_m$ for $[Ca^{2+}]_{subSR}$ tends to saturate at low and high $[Ca^{2+}]_{SR\text{-}release}$ values. The RyR parameters were fitted to provide $Ca^{2+}$ release and $Ca^{2+}$ transients comparable to those in our experiments. The size of the SR and the amount of calsequestrin were fitted to reproduce the $Ca^{2+}$ storing capacity as evaluated by experimentally determined caffeine-induced $Ca^{2+}$ transients.

## Cytosol

$Ca^{2+}$ diffusion between the SL and the perinuclear SR is amplified with local calcium-induced calcium releases (CICRs) (see Results). The $Ca^{2+}$ travels thus via fire-diffusion-fire propagation (35). The model for the fire-diffusion-fire $Ca^{2+}$ propagation is

$$\frac{\partial c}{\partial t} = \beta_i\left[D_{\text{Ca-cytosol}}\nabla^2 c + J_{\text{release}}(r,c) - J_{\text{uptake}}(r,c) + J_{\text{Ca}}\right], \tag{6}$$

where $c$ is $[Ca^{2+}]_i$, $r$ is the spatial coordinate in cytosol, $\beta_i$ is the function determining $Ca^{2+}$ buffering, $D_{\text{Ca-cytosol}}$ is the diffusion coefficient of $Ca^{2+}$ in cytosol, and $J_{Ca}$ is the SR $Ca^{2+}$ flux when $r$ is $r_{SR}$, the SL $Ca^{2+}$ flux when $r$ is $r_{SL}$, and zero with other values. $J_{release}$ and $J_{uptake}$ are the release and uptake $Ca^{2+}$ fluxes at each spatial release site between the SR and SL (35,36). However, due to the lack of experimental data on $Ca^{2+}$ dependence, spatial distribution, activation and inactivation kinetics, and the rate of $Ca^{2+}$ uptake and release fluxes at the spatial release sites ($J_{release}$ and $J_{uptake}$), the models for these release sites would require several equations and parameters without experimental justification. Thus, we simplify the $Ca^{2+}$ diffusion equation to

$$\frac{\partial c}{\partial t} = \beta_i\left[D_{\text{Ca}}\nabla^2 c + J_{\text{Ca}}\right], \tag{7}$$

where

$$D_{\text{Ca}} = \frac{J_{\text{release}}(r,c) - J_{\text{uptake}}(r,c)}{\nabla^2 c} + D_{\text{Ca-cytosol}} \tag{8}$$

and $D_{Ca}$ is fitted to a single numerical parameter ($D_{Ca}$ = 7 $\mu m^2$/ms (see Table 5)) based on our data on the $Ca^{2+}$ propagation velocity in cytosol. The $D_{Ca}$ in this study, therefore, does not represent the diffusion coefficient of free $Ca^{2+}$ diffusion in the cytosol ($D_{\text{Ca-cytosol}}$), but also includes the average CICR-induced (ryanodine-sensitive (see Fig. 6)) amplification of the diffusion (left term of the sum on the right of Eq. 8). Equation 7 is used in spherical coordinates with the radial symmetry assumption in the model cell (see Appendix).

In the cytosol, $Ca^{2+}$ is buffered with troponin C (TnC) and calmodulin (CMDN), which were assumed to be stationary. In neonatal rat ventricular myocytes, the cytosolic $Ca^{2+}$ buffering capacity is significantly smaller than in adult rat ventricular myocytes (37). During cardiomyocyte development, the lower cytosolic $Ca^{2+}$ buffering capacity is caused mostly by a lower TnC concentration (38). If the amount of TnC is considered to depend on the amount of myofibrils, the cultured rat neonatal ventricular myocytes contain 40–64% of TnC/cell volume compared to freshly isolated adult rat ventricular myocytes (15,39). Based on these data, we used 50% of the value for TnC concentration compared to the estimate of 70 $\mu$M generally used in myocyte models (7). In some simulations, the cytosolic $Ca^{2+}$ buffering to 1 mM EGTA was simulated using previously published kinetic parameters (40). Since $Ca^{2+}$ binding to EGTA is very slow compared to other $Ca^{2+}$ buffers in cytosol, we did not use the rapid buffering approximation for EGTA (1,7).

## Simulations of the model

Our model is a combined system of one partial differential equation (PDE) and a system of ordinary differential equations (ODEs). In simulations, the PDE part of the model was approximated to a system of ODEs (see Appendix). Thus, we were able to simulate the complete model with the "ode15s" Matlab 6.5 (The MathWorks, Natick, MA) solver for stiff ODEs. The simulation results were analyzed with Origin 7.5 (OriginLab, Northampton, MA) and Matlab 6.5 (The MathWorks).

The model was driven by a 1-Hz stimulus current ($I_{stim}$, −80 pA/pF, 0.5 ms), except in Figs. 2 and 3, where the cell model or models of individual ion channels were driven with the voltage-clamp protocol. The stimulus current was set to be carried by $K^+$ ions (41). The model was driven to the steady state by applying the stimulus until the intracellular ion concentrations were stable. The temperature and the extracellular ion concentrations were the same as in our experiments (32°C = 305 K, $[Na^+]_o$ = 154.578 mM, $[K^+]_o$ = 5.366 mM, $[Ca^{2+}]_o$ = 1.796 mM) unless stated otherwise.

The effects of ryanodine (50 $\mu$M) and nifedipine (10 $\mu$M) were simulated by setting RyR $Ca^{2+}$ flux and $I_{CaL}$, respectively, to zero. The effect of caffeine (10 mM) was simulated by setting the diffusion rate of RyR $Ca^{2+}$ flux to a large constant value (see Appendix). The SERCA $Ca^{2+}$ flux was set to zero as the $Ca^{2+}$ is extruded almost completely with SL mechanisms when caffeine is applied to cardiomyocytes (1). The increment of diffusion distance was simulated by increasing the $r_{SL}$, whereas the nucleus and SR dimensions remained constant. The SL ion current densities (current/membrane area) were kept constant.

## Data analysis

Data analysis was made using Clampfit 9.2 (Axon Instruments), Origin 7.5 (OriginLab) and Matlab 6.5 (The MathWorks). Matlab's second-order Butterworth low-pass filter was used when necessary in the analysis of $Ca^{2+}$ recordings. Decay of the $Ca^{2+}$ transient was defined as the time required for 2/3 decline of the $Ca^{2+}$ transient amplitude. The experimental data is expressed as the mean ± SE.

# RESULTS

## Action potential

The major difference between APs of adult and neonatal rat ventricular myocytes is the significantly longer repolarization phase in neonatal cells (~150–300 ms) compared to adult cells (~50–70 ms) ((42), our data in Fig. 4 *A* and Table 1, and data in the literature (20,28,43)). The simulated AP of the cultured neonatal rat ventricular myocyte is initiated by $I_{Na}$ peaking at −78.9 pA/pF (Fig. 4, *B* and *C*). This triggers an AP with an amplitude of 92.0 mV, in line with our experimental result (Table 1). The depolarization activates the L-type $Ca^{2+}$ current, which further depolarizes the cell membrane and initiates $Ca^{2+}$ intrusion to the cell (Fig. 4 *C*). Although a significant amount of functional T-type $Ca^{2+}$ current is present in the model cell (Fig. 2 *B*), it plays a minor role compared to the L-type $Ca^{2+}$ current in shaping the simulated AP (Fig. 4 *C*). The net $Ca^{2+}$ intrusion via the T-type $Ca^{2+}$ channel is 7.7% of the $Ca^{2+}$ intrusion via the L-type $Ca^{2+}$ channel. In addition to the $I_{CaL}$, NCX provides a significant $Ca^{2+}$ intrusion (69% compared to $I_{CaL}$) to the cell from 0 to 182 ms in the beginning of the AP (Fig. 4 *C*). In addition to the actively regulated $Ca^{2+}$ intrusion, neonatal cardiomyocytes have a background $Ca^{2+}$ current, the magnitude of which is −0.15 pA/pF or less over the cycle. However, even though the magnitude of $I_{Cab}$ is small, the integral of $Ca^{2+}$ intrusion via $I_{Cab}$ is

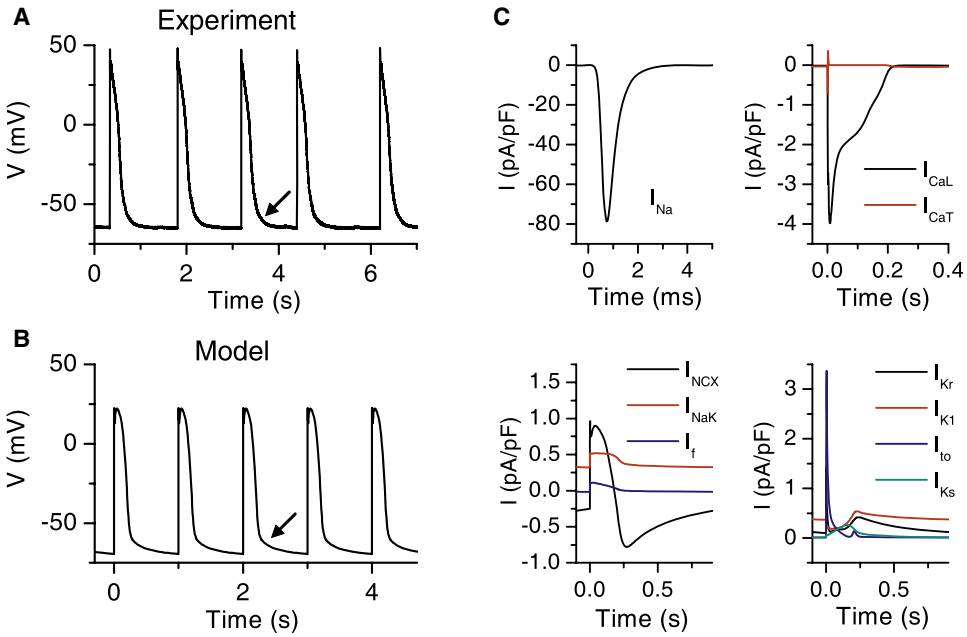


FIGURE 4 Action potential features and contributing currents of the neonatal cardiomyocytes. (*A*) Trace of APs recorded from a spontaneously beating rat neonatal cardiomyocyte culture. (*B*) Trace of simulated APs from 1-Hz pacing of the cell model. In *A* and *B*, the arrows indicate the slow repolarization at the end of the experimental and simulated AP. (*C*) Underlying simulated SL membrane ion currents during AP (see text and Fig. 1 legend for abbreviation definitions).

large, since the current is constantly active throughout the ECC cycle. Taken together, the fractions for $Ca^{2+}$ intrusion are 32.0% ($I_{NCX}$ in the $Ca^{2+}$ intrusion mode), 46.6% ($I_{CaL}$), 3.6% ($I_{CaT}$), and 17.7% ($I_{Cab}$). The SL $Ca^{2+}$ intrusion via these channels is balanced by the $I_{NCX}$ in the $Ca^{2+}$ extrusion mode. This occurs 182 ms from the beginning of the AP, when the $I_{NCX}$ generates a negative depolarizing current (Fig. 4 *C*).

The $K^+$ currents involved in the repolarization of the simulated AP are $I_{Kr}$, $I_{K1}$, $I_{to}$, and $I_{Ks}$ (Fig. 4 *C*). These currents produce a simulated AP repolarization and duration comparable to those in our experimental data (Fig. 4, *A* and *B*, and Table 1). The AP durations at 25, 50, and 80% repolarization ($APD_{25}$, $APD_{50}$, and $APD_{80}$) are in agreement with the experimental values. Also, the slow repolarization phase at the very end of the experimental AP is reproduced in the simulated APs (Fig. 4, *A* and *B*). The simulated $I_{to}$ activates rapidly and provides a repolarizing peak current of 3.4 pA/pF at 3.6 ms after initiation of the AP (Fig. 4 *C*). The $I_{Ks}$ starts to activate slowly at the very beginning of the AP and reaches its maximum of 0.26 pA/pF at 154 ms, after which $I_{Ks}$ is inactivated. The amplitude of $I_{Ks}$ is small and has a minor impact on the APD; without $I_{Ks}$ $APD_{50}$ is 37 ms longer than in the normal cell (data not shown). The $I_{Kr}$ and $I_{K1}$ show similar activity at the end-phase of the repolarization of the AP, with maximum values of 0.42 pA/pF and 0.54 pA/pF, respectively, at 220–230 ms. After the AP is repolarized, $I_{Kr}$ inactivates, whereas $I_{K1}$ remains active at negative membrane potentials, thus contributing to the RP regulation. Other contributors to the RP are the $I_{NCX}$, $I_{NaK}$, and the background $Ca^{2+}$ and $Na^+$ currents (data not shown). The simulated RP (−69.4 mV) is in agreement with our experimental data (Table 1). In addition to the RP regulation, the main function of the $I_{NaK}$ is to maintain the intracellular $Na^+$ and $K^+$ concentrations at physiologically relevant values of 13.8 mM and 151 mM, respectively. The simulated $[Na^+]_i$ is in line with the experimental values of 15.1 ± 4.0 mM and 11.3 ± 5.0 (44) and ~16 mM (estimated from Fig. 4 *B* of Hayasaki-Kajiwara et al. (45)). The high $[Na^+]_i$ explains the large amount of $Ca^{2+}$ intrusion via NCX (1,46). We further estimated the possible effect of the $Ca^{2+}$ buffer EGTA, present in the patch-clamp pipette, on our AP characterization. Based on our simulation, however, EGTA makes only a minor contribution to the AP parameters (Table 1).

The individual neonatal cells are quiescent, but after a few days of culturing, the confluent culture of cells shows rhythmic contractions. Our model cell was also quiescent, because the steady-state activation range and the amount of the pacemaker current ($I_f$) (Fig. 3 *B*) (23,24) are such that $I_f$ makes no contribution to the RP, nor is it capable of triggering spontaneous action potentials or even detectable $V_m$ depolarizations. Since the modeled electrophysiological properties of the cell membrane represent the averages of those defined experimentally (see Methods), this might

**TABLE 1 Simulated and experimental action potential parameters**

| Magnitude | Model | (+ EGTA) | Experiment |
|---|---|---|---|
| RP | −69.4 mV | (−64.1 mV) | −67.1 ± 1.9 mV ($n$ = 10) |
| Action potential amplitude | 92.0 mV | (82.0 mV) | 87.8 ± 5.3 mV ($n$ = 15) |
| $APD_{25}$ | 153.9 ms | (135.6 ms) | 122.9 ± 10.8 ms ($n$ = 15) |
| $APD_{50}$ | 192.7 ms | (218.0 ms) | 197.1 ± 12.1 ms ($n$ = 15) |
| $APD_{80}$ | 232.6 ms | (246.4 ms) | 264.3 ± 13.4 ms ($n$ = 15) |

suggest that in culture only a small fraction of cells are differentiated enough to initiate APs spontaneously, which would then spread in culture and trigger the APs in the quiescent cells. In line with this, most of the neonatal ventricular myocytes are quiescent when cultured individually or at a sparse density (47–49).

### $Ca^{2+}$ diffusion and SR $Ca^{2+}$ release

In adult ventricular cardiomyocytes, the voltage-activated $Ca^{2+}$ channels at the SL and at the invaginations of the SL (T-tubules) are spatially tightly coupled with the RyRs of the SR. This provides a rapid three-dimensionally uniform CICR in the whole cardiomyocyte (1). The neonatal cells, especially when cultured on laminin dishes, lack a proper T-tubule system (1,15). Thus, in neonatal cells, the SL ion channels are located almost completely at the non-T-tubule surface of the SL. On the other hand, based on the immunostaining of SR proteins SERCA2a (16) and RyR (50), the majority of SR is located far from the SL on the perinuclear area. Therefore, the $Ca^{2+}$ entering via the SL has to diffuse a relatively long distance to activate $Ca^{2+}$ release from the SR.

We recorded the spatial distribution of $Ca^{2+}$ within the cultured neonatal rat cardiomyocyte at the time of electrical excitation. We found that the $Ca^{2+}$ entering the cell via the SL during an AP diffuses 4.5 ± 0.8 $\mu$m at a velocity of 0.31 ± 0.07 $\mu$m/ms ($n = 4$) in the cytosol (Fig. 5 *A*). A similar diffusion velocity (0.269 ± 0.015 $\mu$m/ms) has been measured in atrial cardiomyocytes (51), which also lack T-tubules. In the model, the diffusion distance between the SR and SL (4.5 $\mu$m) and the $Ca^{2+}$ diffusion velocity (0.30 $\mu$m/ms) agree with the experimental values. With this speed of diffusion, it takes 15 ms before the SL $Ca^{2+}$ influx initiated by the AP reaches the surface of the SR and triggers the SR $Ca^{2+}$ release (Fig. 5 *B*). To obtain this diffusion velocity, the diffusion coefficient ($D_{Ca}$) was set to 7 $\mu m^2$/ms, which is 10-fold in order of magnitude compared to the $D_{Ca}$ in water (0.79 $\mu m^2$/ms (52)) or that estimated to be in cytosol (~1/2 the $D_{Ca}$ in water (53)). This might suggest that the $Ca^{2+}$ diffusion in the cultured rat neonatal myocytes is amplified by smaller local CICRs during the $Ca^{2+}$ propagation, as in adult atrial myocytes (1,51,54). The amplitudes of sub-SL and sub-SR $Ca^{2+}$ transients were equal in the experiments, as the average amplitude relation (SL/SR) was 0.98 ± 0.02 ($n = 4$). This feature is reproduced in our model as the same relation in simulation is 0.93. The absolute values for simulated $[Ca^{2+}]_i$ are ~0.2 $\mu$M in diastole and ~0.7 $\mu$M in systole. These values are in line with the general estimates of absolute $[Ca^{2+}]_i$ in cardiac muscle cells (1).

From the line-scan images of radial $Ca^{2+}$ concentration (Fig. 5, *A* and *B*) in both the experiment and the model simulation, the last region where $Ca^{2+}$ concentration reaches the maximum (*red*) is located halfway between the SR and SL. This suggests that after a small amount of $Ca^{2+}$ has diffused to the sub-SR region from SL, it induces a $Ca^{2+}$ release from

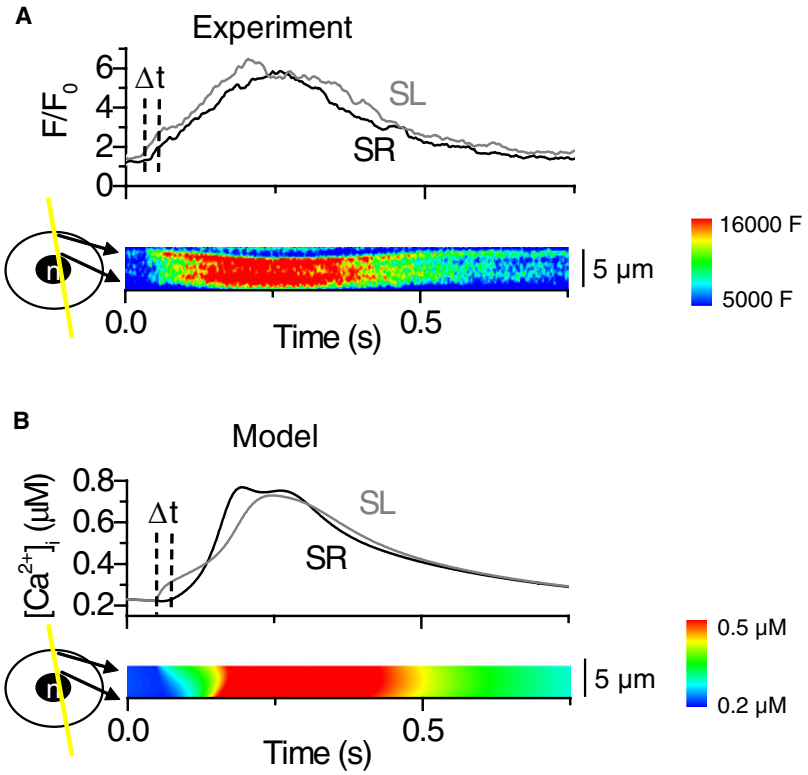


FIGURE 5 Spatiotemporal distribution of the cytosolic calcium during excitation. (*A*) Line-scan recording of $Ca^{2+}$ diffusion within the cytosol. The contour plot shows the radial distribution of cytosolic $Ca^{2+}$ in a single cardiomyocyte after electrical excitation of the cell. (*B*) The experimental recording reproduced by the model. The contour plot shows the simulated cytosolic $Ca^{2+}$ after electrical stimulation of the model cell. The upper panels in *A* and *B* show the traces of $Ca^{2+}$ signals near the SR and nuclear region (*SR*, *black line*) and near the cell membrane (*SL*, *gray line*). Dashed vertical lines indicate the time delay for the $Ca^{2+}$ diffusion from sub-SL to sub-SR.

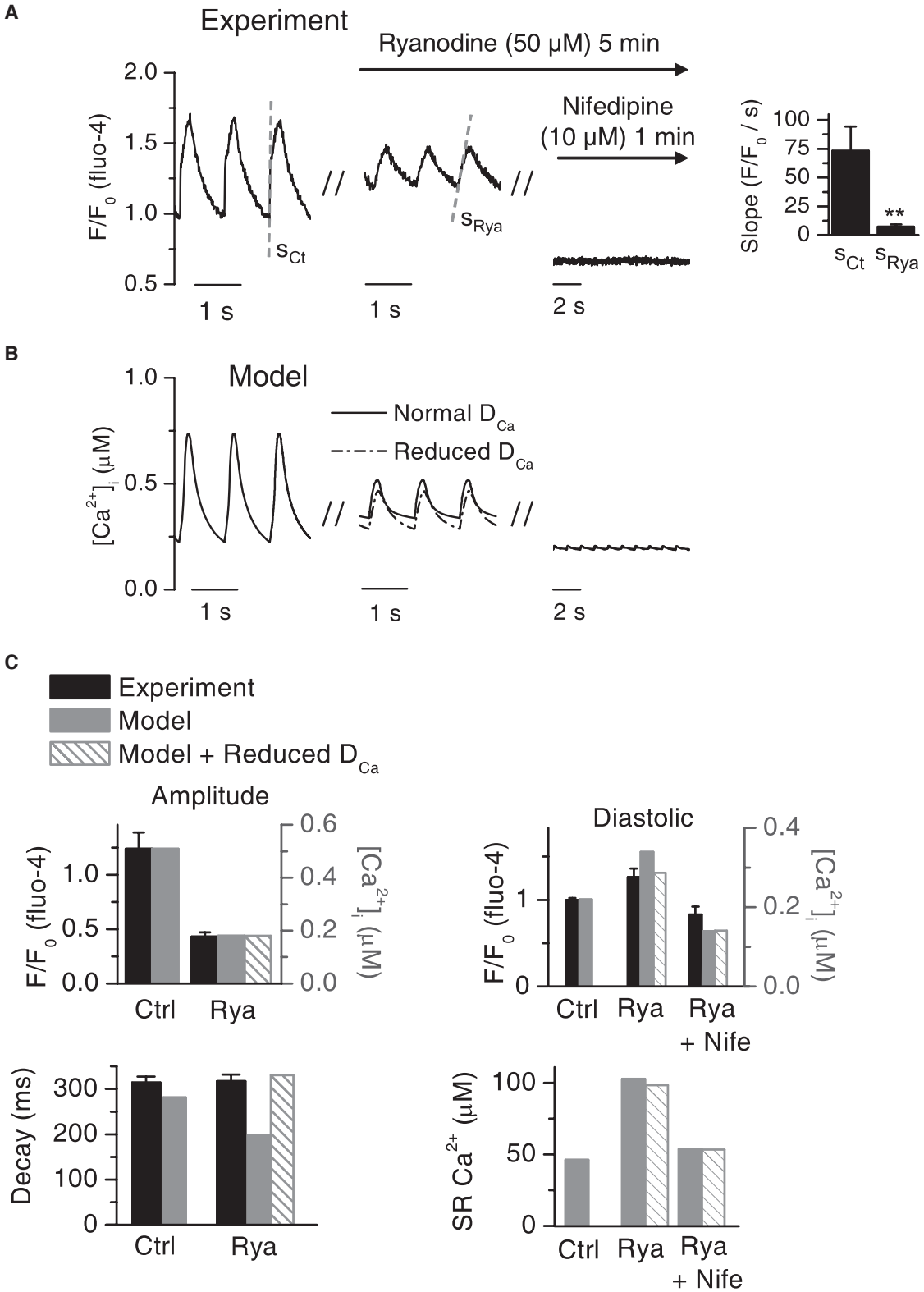


FIGURE 6 The experimental and simulated effects of ryanodine and nifedipine on the cytosolic $Ca^{2+}$ signals. (*A*) Average cytosolic $Ca^{2+}$ was recorded from a single cardiomyocyte during 1-Hz pacing using the line-scan method (*left*). The middle panel shows the $Ca^{2+}$ signal from the same cell after 5 min perfusion of ryanodine (50 $\mu$M). After this, the ryanodine perfusion was continued with nifedipine (10 $\mu$M), and after 1 min of perfusion, the $Ca^{2+}$ signal was recorded from the same cell (*right*). The average value of the initial slope of the $Ca^{2+}$ transient (*dashed gray line*) in control conditions and after exposure to ryanodine (*right*, $n = 14$, $^{**}p < 0.01$). (*B*) The experiment was reproduced by simulation with the model (see Methods). The effects of ryanodine and ryanodine + nifedipine were simulated with the $D_{Ca}$ fitted to our data (*normal*, *solid line*) and with the $D_{Ca}$ in water (*reduced*, *dash-dotted line*). The figure shows the

the SR via RyRs. Subsequently, for a period of time during excitation, $Ca^{2+}$ enters the cytosol from both the SL and SR sides and diffuses from these sources toward the central region of the cytosol.

In adult rat ventricular myocytes, ~90% of the $Ca^{2+}$-transient $Ca^{2+}$ is released from the SR (1), and subsequently, inhibition of SR release by blocking SERCA suppresses cell shortening by 90% (55). Cultured rat neonatal ventricular myocytes express the necessary proteins for SR $Ca^{2+}$ storing (33), release (50), and uptake (16) and therefore, neonatal cells are capable of producing SR $Ca^{2+}$ release, but this release is not very well developed, nor is it a prerequisite for cytosolic $Ca^{2+}$ transients. For example, neonatal cardiomyocytes with genetically downregulated SERCA2 expression generate $Ca^{2+}$ transients upon electrical excitation by $Ca^{2+}$ influx through the SL (16). To verify the contribution of $Ca^{2+}$ release from the SR to the cytosolic $Ca^{2+}$ transients, we recorded the average cytosolic $Ca^{2+}$ signals while modifying the $Ca^{2+}$ sources to cytosol. A large concentration of ryanodine (50 $\mu$M) was used to inhibit SR $Ca^{2+}$ release via RyR. The cells lacking SR $Ca^{2+}$ release showed on average 0.37 $\pm$ 0.04-fold $Ca^{2+}$-transient amplitude and 1.3 $\pm$ 0.1-fold diastolic $[Ca^{2+}]_i$ compared to control conditions (Fig. 6, *A* and *C*). Thus, the SR $Ca^{2+}$ release plays a significant role in the $Ca^{2+}$ signaling of neonatal myocytes, but the cells are also capable of producing competent $Ca^{2+}$ signals with only SL $Ca^{2+}$ influx. The $Ca^{2+}$ signals in the cells with inhibited SR $Ca^{2+}$ release were immediately stalled with the application of the L-type $Ca^{2+}$ channel blocker nifedipine (Fig. 6 *A*). The application of nifedipine also reduced the diastolic $[Ca^{2+}]_i$ to, on average, 0.83 $\pm$ 0.09-fold that of controls (Fig. 6 *C*, *upper right*).

The model cell produced $Ca^{2+}$ signals without SR $Ca^{2+}$ release via RyR (Fig. 6 *B*), just like neonatal cardiomyocytes in the experiments. When the RyRs are blocked, the model cell provides the $Ca^{2+}$ intrusion to the cytosol via the L-type $Ca^{2+}$ channel and NCX. The simulated effect of ryanodine produced a decrease in $Ca^{2+}$-transient amplitude (0.35-fold) and increase in diastolic $[Ca^{2+}]_i$ (1.5-fold) similar to those of the experiments (Fig. 6 *C*). The simulation of the concerted effect of nifedipine and ryanodine inhibited the $Ca^{2+}$ signals and reduced diastolic $[Ca^{2+}]_i$ (0.64-fold), as in the experiments (Fig. 6 *C*). In these conditions, the $Ca^{2+}$ intrusion via NCX at positive membrane voltages is also reduced significantly as the inhibition of the L-type $Ca^{2+}$ channel extinguishes the plateau phase of the AP (data not shown).

It has been suggested that in atrial myocytes, propagation of the $Ca^{2+}$ signal within the cytosol is amplified by local CICRs (54). In support of this suggestion, $Ca^{2+}$ diffusion velocity in the cytosol is reduced if SR $Ca^{2+}$ releases are inhibited (51). In the global $Ca^{2+}$ transient, the amplified $Ca^{2+}$ diffusion accounts for the initial slope, whereas the $Ca^{2+}$ release from the central regions of the cell accounts for the secondary slower component (54). Just as in atrial myocytes, the upstroke of the $Ca^{2+}$ transients of neonatal cardiomyocytes has two distict components (Fig. 6 *A*), as well as a distinct diffusion pattern in the linescan images (Fig. 5 *A*), suggesting that cytosolic $Ca^{2+}$ diffusion and $Ca^{2+}$ release in neonatal cardiomyocytes might resemble those in atrial myocytes. In addition, the $Ca^{2+}$ diffusion velocity of the neonatal cells is significantly higher than expected. We therefore tested whether inhibition of CICR reduces the $Ca^{2+}$ diffusion velocity in neonatal myocytes in a manner similar to that in atrial cardiomyocytes (51). When we inhibited the CICR with ryanodine, not only was the amplitude of the calcium transients decreased, but also the slope of the $[Ca^{2+}]$ rise was reduced by ~85%, suggesting that $Ca^{2+}$ diffusion might be amplified by propagating local CICRs (Fig. 6 A). Based on this, we tested in our model how the altered diffusion velocity changes the global $Ca^{2+}$ signals. We ran the same RyR and RyR + $I_{CaL}$ block simulations as described above, with the $D_{Ca}$ reduced to the value in water (0.79 $\mu m^2$/ms (52)), simulating nonamplified diffusion. With the reduced $D_{Ca}$ we obtained better agreement between our simulated and experimental results for the effects of ryanodine. The decay of the $Ca^{2+}$ did not decrease as it did with normal $D_{Ca}$ (Fig. 6 *C*). In fact, the decay increased slightly with reduced $D_{Ca}$, suggesting that some of the amplified diffusion might have been still present in the experiment. Also the diastolic $Ca^{2+}$ with ryanodine compared better with the experimental value when we used the reduced $D_{Ca}$ (Fig. 6 *C*). Other simulated $Ca^{2+}$ signaling parameters were the same with normal and reduced $D_{Ca}$ (Fig. 6 *C*).

The simulated inhibition of SR $Ca^{2+}$ release leads to the accumulation of $Ca^{2+}$ in the SR (Fig. 6 *C*), and consequently, SERCA cannot pump $Ca^{2+}$ against the increased concentration gradient between the SR and cytosol. This leaves NCX as the only possible $Ca^{2+}$ extrusion route during relaxation. Compared to control conditions, where $Ca^{2+}$ is removed from both sides of the cytosol (SERCA and NCX), the $Ca^{2+}$ now has to diffuse a longer distance (from the sub-SR to sub-SL) before it is extruded from the cell. This slows down the $Ca^{2+}$ extrusion and leads to the accumulation of cytosolic $Ca^{2+}$ and increased diastolic $[Ca^{2+}]_i$. Subsequently, when the $Ca^{2+}$ intrusion to the cytosol is reduced significantly with nifedipine, the diastolic $[Ca^{2+}]_i$ decreases (Fig. 6 *C*). The

average cytosolic $Ca^{2+}$ from the simulations. (*C*) The simulated data with normal $D_{Ca}$ (*solid gray bars*) and with reduced $D_{Ca}$ (*gray-hatched bars*) and the average experimental data (*black bars*) from the experiments ($n = 14$). The left panels show the $Ca^{2+}$-transient amplitude and decay in control conditions and after exposure to ryanodine. The upper right panel shows the diastolic $[Ca^{2+}]_i$ in control, with ryanodine, and with ryanodine + nifedipine. The lower right panel shows the simulated diastolic SR $Ca^{2+}$ content in cytosol volume in control, ryanodine, and ryanodine + nifedipine conditions.

reduced cytosolic $Ca^{2+}$ decreases the uptake flux of SERCA, and the SR $Ca^{2+}$ content with ryanodine and nifedipine is returned to near the control value (Fig. 6 C).

The amount of the releasable $Ca^{2+}$ stored in the SR was studied by emptying the SR $Ca^{2+}$ to the cytosol after the SR $Ca^{2+}$ content was normalized with 1-Hz pacing. The SR $Ca^{2+}$ was emptied to the cytosol by the rapid application of 10 $\mu$M caffeine with SL $Ca^{2+}$ intrusion prevented by the simultaneous application of 5 $\mu$M nifedipine. The amplitude of $Ca^{2+}$ transients during 1-Hz pacing was 0.42 $\pm$ 0.05 $F/F_0$ (fluo-3, $n = 9$), and the amplitude of caffeine-induced $Ca^{2+}$ transients was 0.51 $\pm$ 0.05 $F/F_0$ (fluo-3, $n = 9$) (Fig. 7, *A* and *B*). The average ratio for the caffeine/twitch $Ca^{2+}$-transient amplitude was 1.26 $\pm$ 0.06. The SR $Ca^{2+}$ storing capacity in our model is in good agreement with experiments, as the simulated ratio for the caffeine/twitch $Ca^{2+}$-transient amplitude was 1.25 (Fig. 7, *A* and *B*).

The functional amount of cytosolic $Ca^{2+}$ extrusion mechanisms, the SERCA in the surface of the SR and NCX in the surface of the SL, can be analyzed by observing the decay of the $Ca^{2+}$ transients. The $Ca^{2+}$ released during the caffeine-induced $Ca^{2+}$ release is removed completely by NCX (1). The experimental and simulated $Ca^{2+}$ extrusion capacities of the NCX are in good agreement, as caffeine-induced $Ca^{2+}$ transients have the same decay in both (Fig. 7 *B*). During a normal twitch, both SERCA and NCX are active. The extrusion capacity of SERCA is correct in our model, as SERCA and NCX (whose value in the model was fixed with the caffeine experiment) together produce a $Ca^{2+}$ transient decay during a normal 1-Hz twitch similar to that of the real cells in our experiments (Fig. 7 *B*).

During one simulated 1-Hz $Ca^{2+}$ transient, 17% of the SR $Ca^{2+}$ content is released to the cytosol (Fig. 8, *A* and *B*). The $[Ca^{2+}]_{SR}$ decreases mostly at the release compartment. This decrease inactivates the release as the open probability of the RyR model is regulated by the $[Ca^{2+}]_{SRrelease}$. The SERCA flux follows tightly the changes in cytosolic $Ca^{2+}$ but is saturated at the highest cytosolic $Ca^{2+}$ concentrations (Fig. 8 *B*). The uptaken cytosolic $Ca^{2+}$ is diffused from the SR uptake compartment back to the SR release compartment ($J_{tr}$ in Fig. 8 *B*). The $[Ca^{2+}]_{SRuptake}$ decreases less than the $[Ca^{2+}]_{SRrelease}$ because of the delay in diffusion between these compartments. The magnitude of passive $Ca^{2+}$ leak from the SR to the cytosol is almost negligible compared to the RyR and SERCA $Ca^{2+}$ fluxes (Fig. 8 *B*), as the SR $Ca^{2+}$ content is balanced with the more realistic SERCA backflux rather than with an unrealistically large passive leak (32).

The net $Ca^{2+}$ fluxes between the SL and cytosol ($J_{CaL} + J_{CaT} + J_{Cab} - J_{NCX}$) and between the SR and cytosol ($J_{RyR} + J_{leak} - J_{SERCA}$) maintain the $Ca^{2+}$ homeostasis during one cycle (Fig. 9 *A*). Activation of the SL sources produces 10.5 $\mu$M $Ca^{2+}$ intrusion to the cell, whereas activation of the SR sources produces 7.9 $\mu$M $Ca^{2+}$ intrusion to the cell. During relaxation, the same amounts of $Ca^{2+}$ are removed from the cytosol to the corresponding $Ca^{2+}$ sources. Even though the amplitude of the simulated $Ca^{2+}$ transient in the presence of ryanodine was 35% that of the control, the amount of $Ca^{2+}$ intruding to the cytosol from SL sources is 57% of the total SR + SL $Ca^{2+}$ intrusion. This difference is mostly due to the limited $Ca^{2+}$ buffering capacity of the myocyte. When some of the buffering capacity of the cytosol is already occupied by the SL-originated $Ca^{2+}$, a smaller amount of SR-originated $Ca^{2+}$ is needed to further increase the free $[Ca^{2+}]_i$ (Fig. 9 *B*). The analysis of free and buffered $Ca^{2+}$ is further complicated by the spatial differences within the cytosol.

## Increment of cytosol size in hypertrophy

An increase in cell size (hypertrophy) is involved in the development of cardiac failure (1). Although there are

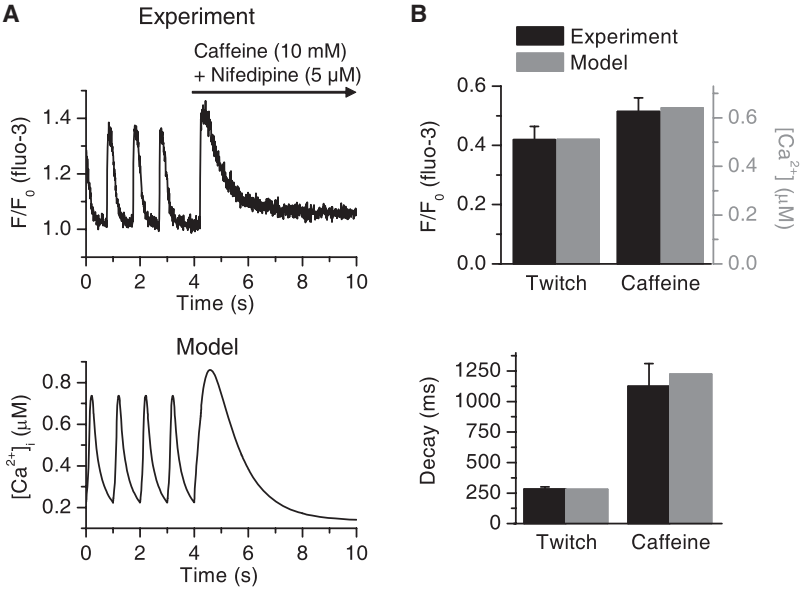


FIGURE 7 SR calcium stores of the neonatal cardiomyocytes. (*A*, *upper*) Cytosolic $Ca^{2+}$ signal recorded from a single cell during 1-Hz electrical excitation. At 4 s, the pacing was stopped and caffeine (10 mM) and nifedipine (5 $\mu$M) were rapidly applied to the dish via the perfusion system. (*Lower*) Average cytosolic $Ca^{2+}$ signal of the model when the experiment was reproduced in simulations. The model was paced at 1 Hz and at 4 s, the effect of caffeine and nifedipine was simulated (see Methods) with the pacing halted. (*B*) The parameters of $Ca^{2+}$ transients from simulated data (*gray*) and from the experimental data (*black*, $n = 9$). (*Upper*) Normal and caffeine-induced twitch $Ca^{2+}$-transient amplitudes. (*Lower*) Decays of the $Ca^{2+}$ transients.

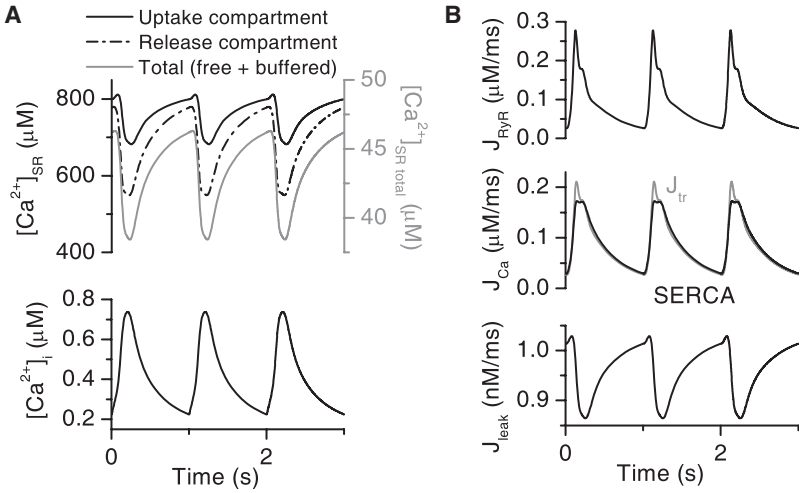


FIGURE 8 Simulated $Ca^{2+}$ fluxes and $Ca^{2+}$ content of the neonatal myocyte. (*A*) The average cytosolic $Ca^{2+}$ transients (*lower*) compared to the corresponding SR $Ca^{2+}$ concentration in the uptake compartment (*solid black line*) and in the release compartment (*dash-dotted black line*) during 1-Hz pacing of the model cell. The total (free + buffered) SR $Ca^{2+}$ content in the cytosol volume is also plotted (*gray solid line*). (*B*) The underlying SR $Ca^{2+}$ fluxes of the cytosolic and SR $Ca^{2+}$ signals: $Ca^{2+}$ release flux via RyR (*upper*), the SERCA uptake flux (*black line* (*middle*)) and the $Ca^{2+}$ diffusion flux from $SR_{uptake}$ to $SR_{release}$ ($J_{tr}$, *gray line* (*middle*)), and the $Ca^{2+}$ leak flux from $SR_{uptake}$ to cytosol (*lower*). The $Ca^{2+}$ fluxes are within the cytosol volume.

many discrepancies between the analyzed phenotypes of hypertrophied myocytes, changes generally observed in ECC are reduced $Ca^{2+}$ transient amplitude and relaxation, reduced SR $Ca^{2+}$ content, and prolonged APs. These changes are explained by altered gene expression levels and phosphorylation status of ECC proteins (1). Similar phenotypes and explanations have been reported in several studies where hypertrophy and underlying signaling cascades were studied in cultured rat neonatal ventricular myocytes (28,56,57). In addition to the changes in gene expression and ECC protein function, one aspect that must be considered in hypertrophied cultured neonatal myocytes is the change in cell geometry and dimensions. Neonatal myocytes lack the spatial coupling of $I_{CaL}$ and RyR, and thus the $Ca^{2+}$ has to diffuse between the SL and SR surface for the CICR to occur (Fig. 5). This diffusion distance increases as the myocyte becomes hypertrophied. When we included the spatial dimension to cytosolic $[Ca^{2+}]$ in our model, we were able to simulate how the change in the $Ca^{2+}$ diffusion distance between the SR and SL affects the ECC in cultured neonatal myocytes.

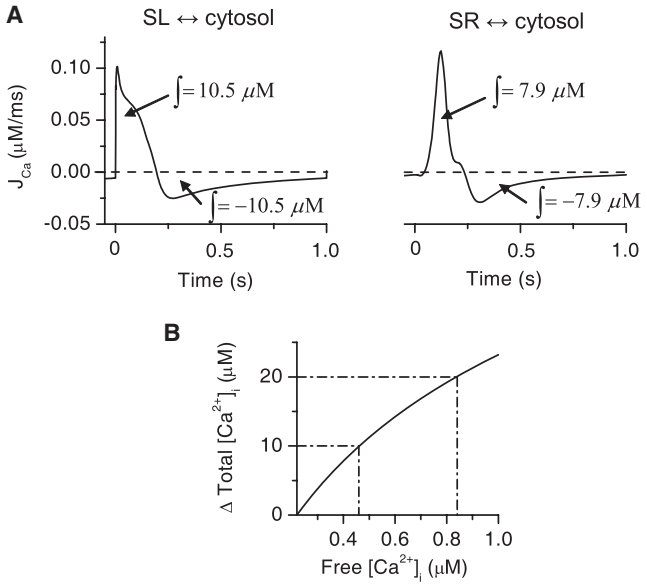


FIGURE 9 Simulated contributions of calcium fluxes to cytosolic $Ca^{2+}$ transients of the neonatal cardiomyocytes. (*A*) The simulated net $Ca^{2+}$ fluxes during one ECC cycle between the extracellular space (*SL*) and cytosol ($J_{CaL} + J_{CaT} + J_{Cab} - J_{NCX}$ (*left*)) and between SR and cytosol ($J_{RyR} + J_{leak} - J_{SERCA}$ (*right*)). The integrals of the fluxes during activation and relaxation are shown in the figure. The concentrations are in cytosol volume. (*B*) The increment of total cytosolic $Ca^{2+}$ content compared to the free $[Ca^{2+}]_i$ starting from the diastolic value of free $[Ca^{2+}]_i$. The dash-dotted lines indicate the nonlinearity of the increment in free $[Ca^{2+}]_i$ between the 0–10 $\mu$M and 10–20 $\mu$M increments in the total cytosolic $Ca^{2+}$.

One obvious change in $Ca^{2+}$ signaling when increasing the diffusion distance between the SL and SR is the increased diffusion time from the SL to SR (Fig. 10 *A*), which subsequently delays the activation of CICR. Increasing the diffusion distance causes several changes in the average cytosolic $Ca^{2+}$ signals, which resemble those seen in hypertrophied myocytes. The amplitude of the $Ca^{2+}$ transient decreases dramatically as the diffusion distance increases, leading to reduced contraction force. The decay of the $Ca^{2+}$ transient increases, which leads to an increase in diastolic $Ca^{2+}$ as the diastolic interval is too short for complete relaxation of the $Ca^{2+}$ signal. The AP was slightly prolonged and the resting potential increased when the diffusion distance increased (14% and 4% increase, respectively, between 4.5 $\mu$m and 9 $\mu$m distance (Fig. 10 *C*)). The absolute SR $Ca^{2+}$ content (the concentration in SR volume) did not change (Fig. 10 *D*). When scaling the SR $Ca^{2+}$ content to the cytosol volume, as is done in experimental determination of SR $Ca^{2+}$ content (Fig. 7) (1), the SR $Ca^{2+}$ content decreases when the diffusion distance, and thereby the cytosolic volume, increases. In general, these results show that in addition to the altered gene expression levels, the phenotype of hypertrophied and failing cultured rat neonatal ventricular myocytes is shaped by the increased diffusion distance between the SL and SR, produced solely by the growth of the cells.

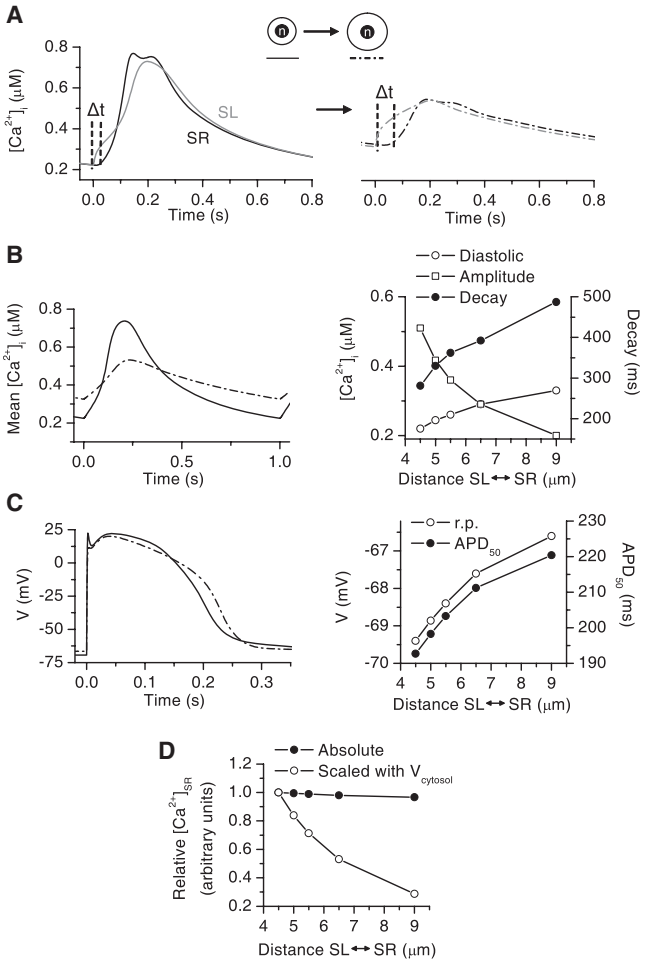


FIGURE 10 Simulated effect of the increase in diffusion distance between SL and SR on $Ca^{2+}$ signaling and APs. (*A*) The sub-SR (*black*) and sub-SL (*gray*) cytosolic $Ca^{2+}$ signals in a normal cell (*left*) and in a cell with a twofold diffusion distance (*right*). The $\Delta t$ indicates the time delay in $Ca^{2+}$ diffusion from the sub-SL to the sub-SR cytosolic region. (*B*) Average cytosolic $Ca^{2+}$ (*left*) in a normal cell (*solid line*) and in a cell with a twofold diffusion distance (*dash-dotted line*). (*Right*) Diastolic $[Ca^{2+}]_i$, $Ca^{2+}$-transient amplitude, and $Ca^{2+}$-transient decay in cells with a diffusion distance between the control value (4.5 $\mu$m) and the twofold value (9 $\mu$m). (*C*) The AP in a normal cell (*solid line*) and in a cell with a twofold diffusion distance (*dash-dotted line*). (*Right*) RP and $APD_{50}$ in cells with a diffusion distance between the control (4.5 $\mu$m) and twofold values (9 $\mu$m). (*D*) The absolute (*black circles*) and cytosol volume scaled (*open circles*) SR $Ca^{2+}$ content in cells with a diffusion distance between the control value (4.5 $\mu$m) and the twofold value (9 $\mu$m). In both cases, the SR $Ca^{2+}$ contents were scaled with the control values. In *A–D*, all phenotypes of the model cell were driven at 1-Hz pacing to the steady state.

## DISCUSSION

In this study, we developed a mathematical model of the excitation-contraction coupling of rat neonatal ventricular myocytes. This study reveals important consequences originating from the unique structural and functional features of the ECC of these cells. The long-AP, heterogeneous cytosolic $Ca^{2+}$ signals and strong SL and weak SR $Ca^{2+}$ cycling produce ECC that differs significantly from those of adult rat and other mammalian ventricular myocytes. These results provide an analysis of the limits of the neonatal cardiomyocyte as a general model of the cardiac cell, as well as information on ECC during cardiomyocyte development.

### Diffusion and heterogeneity of cytosolic $Ca^{2+}$

The most important and unique structural feature of cultured rat neonatal ventricular myocytes compared to adult cardiomyocytes is the lack of the T-tubule system (1,15). In adult mammalian ventricular cells, the fast, uniform, and efficient SR $Ca^{2+}$ release is based on the tight spatial coupling between the L-type $Ca^{2+}$ channels of the SL and the RyRs of the SR (1). These functional couplings are mostly located at the T-tubules, which are SL invaginations conducting the electrical excitation to the interiors of the cell. This geometric structure ensures simultaneous activation of L-type $Ca^{2+}$ channels and CICR in the 3-D space of the cell, resulting in a uniform cytosolic $Ca^{2+}$ transient. The neonatal ventricular myocytes lack the T-tubule system and consequently the distance between RyRs and voltage-activated $Ca^{2+}$ channels is much longer than in adult ventricular cells (1). This leads to looser coupling and slower dynamics in CICR and less uniform $Ca^{2+}$ signals within the cytosol (Fig. 5).

Several findings of this study propose that $Ca^{2+}$ diffusion between the SL and perinuclear SR might be amplified with local CICRs, as is the case in atrial ventricular myocytes (1,51,54). According to our measurements, the $Ca^{2+}$ diffusion velocity between the perinuclear SR and SL is comparable to the velocity measured in atrial myocytes by Sheehan and Blatter ($0.31 \pm 0.07$ $\mu$m/ms and $0.269 \pm 0.015$ $\mu$m/ms, respectively (51)). To reproduce this diffusion velocity in our model, the diffusion coefficient for $Ca^{2+}$ was fitted to a value ~10-fold that in aqueous solutions and cytosol (7 vs. 0.79 $\mu m^2$/ms (52) and ~$1/2 \times 0.79$ $\mu m^2$/ms (53), respectively). Inhibition of CICR by ryanodine reduced the diffusion velocity in a way similar to that observed in atrial myocytes (54). In the model, the experimental $Ca^{2+}$ signals without possible CICR-amplified diffusion were better reproduced with $D_{Ca}$ reduced to the value in aqueous solutions. Based on these findings, it seems that $Ca^{2+}$ diffusion in the cytosol of neonatal cardiomyocytes might be amplified by the local CICRs.

### Sources of cytosolic $Ca^{2+}$

In adult mammalian ventricular myocytes of most species, $[Na^+]_i$ is in the range 4–8 mM, but for rat and mouse, $[Na^+]_i$ is in the range 10–15 mM (58). Another feature that distinguishes rat and mouse from other mammalian species is the short AP in adult ventricular myocytes (~10–70 ms (42,59) compared to, for example, ~200–360 ms in rabbit, canine, and human cardiomyocytes (60–62)). The high $[Na^+]_i$ in rat and mouse myocytes provides a possibility for $Ca^{2+}$ intrusion via the NCX at high $V_m$ values (1,63),

but due to the short APs, the amount of intruded $Ca^{2+}$ cannot be large. In other mammals, the lower $[Na^+]_i$ prevents the NCX $Ca^{2+}$ intrusion mode, although the long APs could provide a positive $V_m$, which would favor $Ca^{2+}$ intrusion via the NCX. Neonatal cardiomyocytes have a high $[Na^+]_i$ (44,45) and long APs (20,28,43) (Fig. 4 *A* and Table 1), which together favor large and long-lasting $Ca^{2+}$ influx via the NCX. In the simulations of our model, the NCX contributed significantly to the SL $Ca^{2+}$ intrusion during APs. The long AP also prolongs the open time of the L-type $Ca^{2+}$ channel, resulting in a large $Ca^{2+}$ intrusion. In cultured rat ventricular myocytes, the large $Ca^{2+}$ intrusion via SL sources ($I_{CaL}$ and NCX) during APs explains their ability to produce $Ca^{2+}$ signals without SR $Ca^{2+}$ release (16) (Fig. 6).

In contrast to the stronger $Ca^{2+}$ cycling via the SL, the SR $Ca^{2+}$ handling capacity is much weaker in neonatal than in adult rat cardiomyocytes. However, in neonatal cardiomyocytes, SERCA and NCX are still the predominant $Ca^{2+}$ extrusion mechanisms compared to mitochondria and SL $Ca^{2+}$-ATPase (64). Based on experiments and modeling, the SR $Ca^{2+}$ content in the cytosol volume is around two- to threefold smaller in neonatal than in adult rat cardiomyocytes (65–67). Also, the SR $Ca^{2+}$ release and uptake capacity has to be significantly higher in the adult rat, because adult cytosolic $Ca^{2+}$ transients originate almost completely from the SR (55). During each contraction, the adult rat cycles ~78 $\mu$M of $Ca^{2+}$ between the SR and cytosol (based on the fractional release and SR $Ca^{2+}$ content of Delbridge et al. (66)). In our neonatal model, the amount of cycled $Ca^{2+}$ between the SR and the cytosol is ~10% of this value, whereas the total released $Ca^{2+}$ from the SR and SL sources in our neonatal model is only ~24% of the total $Ca^{2+}$ release in adult rat. This smaller amount of $Ca^{2+}$ is still sufficient to activate regular-sized $Ca^{2+}$ transients due to the reduced buffering capacity in neonatal myocytes (see Methods). These numbers should not be considered quantitatively accurate, but they demonstrate roughly how the absolute amount of cycled $Ca^{2+}$ during a twitch and the balance between SR and SL $Ca^{2+}$ cycling is completely different in neonatal rat myocytes compared to adult rat myocytes. Inhibition of the SR and SL $Ca^{2+}$ channels, pumps and exchangers thus produces different effects on the function of adult versus neonatal cardiomyocytes. Due to the smaller cytosolic buffering capacity in neonatal cells, the cytosolic $Ca^{2+}$ signals are less tolerant of interferences in the $Ca^{2+}$ sources. As a result, the activities of the $Ca^{2+}$-dependent enzymatic pathways (68–70), which are essential to directing the cell's phenotype from postnatal to adult ventricular myocyte and to promoting cell growth, are subsequently more easily suppressed by interventions in $Ca^{2+}$ signaling.

## Hypertrophy

The gene expression levels of various $Ca^{2+}$-handling proteins change in hypertrophy and cardiac failure (1) and also in cultured neonatal cardiomyocytes when exposed to growth-promoting agents or conditions (56,57). We hypothesized that apart from the gene expression changes, the growth of the cell itself will have an effect on cell signals in neonatal myocytes, where the spatial $Ca^{2+}$ dynamics in cytosol play a central role in the function of the cell. Based on our simulations, an increased diffusion distance between the SR and SL alone induces changes in the function of the hypertrophic cardiomyocyte that resemble those commonly induced by altered gene expression during the development of pathological hypertrophy (1). The changes are most dramatic in $Ca^{2+}$ signaling, where even a small increase in diffusion distance (from 4.5 $\mu$m to 5 $\mu$m, i.e., an 11% increase) was sufficient to change the $Ca^{2+}$ signaling properties and SR $Ca^{2+}$ content by a physiologically significant magnitude (~10–20%). The increased diffusion distance increases the heterogeneity of cytosolic $Ca^{2+}$ signals and slows down the diffusion through the cytosol. This results in slower activation and relaxation and flattening of the peak of the total average cytosolic $Ca^{2+}$ transient. These changes are usually hallmarks of pathological hypertrophy and cardiomyocyte failure (1). The altered cytosolic $Ca^{2+}$ signal interacts with SL ion channels and prolongs the AP. The magnitude of prolongation of the simulated AP (a 14% increase in $APD_{50}$ with a twofold diffusion distance) was smaller than that reported in hypertrophied rat neonatal myocytes (a 42% increase in $APD_{50}$) (28). This indicates that other changes also take place, such as the reported changes in ion current densities (28). However, based on our simulations, the increase in diffusion distance also contributes to prolonging of the AP. The simulated change in RP was small and nonsignificant, which is in line with the experimental results (28).

Our results show that the increase in diffusion distance alone plays an essential role in shaping the cytosolic $Ca^{2+}$ signals and APs of hypertrophied neonatal cardiomyocytes. For complete modeling of hypertrophy, the relative growth of the nucleus and SR compared to the cytosol should be estimated and included in the model. However, the diffusion distance between the SL and SR ($d = r_{SL} - r_{SL}$ in Fig. 1) always increases in hypertrophy if we assume that the cytosol, nucleus, and SR grow somewhat equally in proportion to each other. For example, a 20% growth (in diameter) of the cell and intracellular structures, regardless of the growth of the SR and nucleus, results in a 20% increase in diffusion distance,

$$d_{\mathrm{Diffusion-Control}} = r_{SL} - r_{SR} \xrightarrow{20\%\ \mathrm{growth}}$$
$$d_{\mathrm{Diffusion-Hypertrophy}} = 1.2r_{SL} - 1.2r_{SR} = 1.2d_{\mathrm{Diffusion-Control}}, \quad (9)$$

which by itself shapes the $Ca^{2+}$ signals and APs in hypertrophied myocytes, as we have shown.

### Limitations of the study

A general problem in developing a model of cultured rat neonatal ventricular myocytes is the large variability in the observed phenotypes of these cells. The different culture conditions (15) and the age of the culture (14) have been shown to change various properties of these cells, such as the physical structure and the number of ion channels. The data used in model development comes from several different laboratories and it cannot be assumed that the culture conditions and times are identical. We cannot overcome the variability in culture conditions, but to minimize the age-related error, we used data obtained from cells cultured for 3–5 days whenever possible, as this is a culture time often used in experimental studies.

To model the measured $Ca^{2+}$ diffusion in cytosol we had to use a higher value for the $Ca^{2+}$ diffusion coefficient than previously reported in aqueous solution or cytosol. The apparent $Ca^{2+}$ diffusion velocity was close to that measured for the $Ca^{2+}$ wave propagation and much faster than free $Ca^{2+}$ diffusion (51–53). One possible contributor to the measured $Ca^{2+}$ diffusion velocity is the geometry of the studied cells (see below) and the direction of the $Ca^{2+}$ wave propagation. When measuring the $Ca^{2+}$ diffusion velocity with confocal line scanning, $Ca^{2+}$ is assumed to diffuse in a vertical direction to the viewer (on the *xy* plane). However, in the 3-D cytosol of real cells, $Ca^{2+}$ also diffuses in a direction parallel to the viewer (the *z*-direction), which will contribute to the 2-D speed of $Ca^{2+}$ propagation in cells. Nevertheless, these measurements give a reasonable estimate of $Ca^{2+}$ propagation in the particular observed 2-D plane within the 3-D cell (18,19,51,71). The model represents this complex phenomenon by means of linear radial diffusion (as in Fig. 5), which was fitted to correspond to the average $Ca^{2+}$ propagation measured with line scanning. These issues related to the geometry of the cell cannot completely explain the high diffusion velocity. In our experiments, inhibition of the RyR did reduce the propagation velocity of the $Ca^{2+}$ signal in cytosol. Based on our experiments, we cannot rule out the possibility that $Ca^{2+}$ diffusion in neonatal cardiomyocytes could indeed be amplified with local CICRs, as reported in atrial cells of different species (1,51,54,72), but more experiments are needed to support our observations.

Modeling $Ca^{2+}$ diffusion between the perinuclear SR and SL was complicated, because of the possibility that the diffusion might be amplified by local CICRs. There is not sufficient data available on $Ca^{2+}$ dependence, spatial distribution, activation and inactivation kinetics, and rate of $Ca^{2+}$ uptake and release flux at the spatial release sites to implement a fire-diffusion-fire model (35,36) of the cell cytosol. On the other hand, approximating $D_{Ca}$ (Eq. 8) with a constant number is not optimal, since $D_{Ca}$ depends on the local release and uptake fluxes and the Laplacian of the local [$Ca^{2+}$]. This is seen when local fluxes are altered (Fig. 6). However, when the limitations are kept in mind, our model is able to reproduce the experimental spatial $Ca^{2+}$ signals at the level of accuracy of the experiments (Fig. 5). We consider that a simple model that can reproduce the experimental data is a better choice than an extremely complex model with several assumptions, equations, and parameters without experimental basis.

The spherical shape of the model cell is a rough estimate of real cells. A more realistic estimation would be a flat ellipsoid, but this would exponentially increase the computational demands of the model. The description of diffusion would require three coordinates compared to the one needed for radial diffusion in a sphere. The $Ca^{2+}$ would then have additional spatial differences in a direction parallel to the SL and SR surfaces, and the function of $Ca^{2+}$-transporting ion channels would need to be calculated separately for all points of the SL and SR surface grid. The use of a spherical shape is thus a fair compromise between computational demand and accuracy of the model.

Despite these limitations, our model reproduces faithfully the ECC of cultured rat neonatal myocytes. The spherical shape and the experimental method of determining the spatial cytosolic $Ca^{2+}$ signals seems to be an accurate approach for analyzing the ECC of these cells. Furthermore, the model has the general features common to all neonatal cells: 1), loose coupling between the RyR and the $I_{CaL}$; and 2), a long AP with strong SL $Ca^{2+}$ influx (1). Thus, it describes qualitatively the ECC in neonatal cells in general. We propose that the experimental and computational methods used here could be also adapted successfully for analyzing the ECC in other developing cardiomyocytes with a similar structure.

## CONCLUSION

In this study, we have characterized the action potentials and $Ca^{2+}$ signaling dynamics underlying the excitation-contraction coupling in cultured rat neonatal ventricular myocytes. We have shown, with experiments and modeling, that important differences exist between neonatal and adult cells. Compared to adult cardiomyocytes, neonatal cardiomyocytes have longer APs, heterogeneous cytosolic $Ca^{2+}$ signals, the SL as a strong $Ca^{2+}$ source with significant contribution via the NCX, and weaker SR $Ca^{2+}$ handling. Structural differences between adult and neonatal cells also exist, and the ECC of these cells may be altered differently by structural changes such as hypertrophy. Distinction of these features will help us to understand the ECC of developing cardiac myocytes, as well as the limitations of cultured rat neonatal and other developing cardiomyocytes as a general model of the cardiomyocyte. Using the results and mathematical model presented here, more detailed studies of ECC can be made with these cell cultures.

We have presented what is to our knowledge the first mathematical model of ECC in rat neonatal ventricular myocytes, with a novel description of the SL membrane currents, SR $Ca^{2+}$ dynamics, and spatial cytosolic $Ca^{2+}$. This model faithfully describes the ECC of these cells and, as presented here,

can be used also to study dysfunctions in ECC. From a more general viewpoint, we have introduced novel issues in myocyte modeling. With the aim of modeling neonatal myocytes reliably, we have developed the first integrated model of AP-generating SL ion currents, spatial cytosolic $Ca^{2+}$ signals, and SR $Ca^{2+}$-handling dynamics. Furthermore, our model is among the first models we know of that describes ECC in the field of developing cardiomyocytes.

## APPENDIX: MODEL EQUATIONS

The model parameters are defined in Tables 2–5. Values in the equations are in units of mV for voltage, $\mu$M for concentrations, pl for volume, ms for time, $\mu$m for distance, pA/pF for current, and $\mu$M/ms (in a 1-pl volume) for fluxes. The scaling factors required for agreement of the units are shown within the equations.

### Nernst potentials

$$E_{Ca} = \frac{RT}{2F}\ln\frac{[Ca^{2+}]_o}{[Ca^{2+}]_{subSL}} \quad (10)$$

$$E_K = \frac{RT}{F}\ln\frac{[K^+]_o}{[K^+]_i} \quad (11)$$

$$E_{Na} = \frac{RT}{F}\ln\frac{[Na^+]_o}{[Na^+]_i} \quad (12)$$

### SL membrane currents

*L-type $Ca^{2+}$ current*

$$I_{CaL} = G_{CaL}dff_{Ca}4\frac{VF^2}{RT}\frac{[Ca^{2+}]_{subSL}e^{2VF/RT} - 0.341[Ca^{2+}]_o}{e^{2VF/RT} - 1} \quad (13)$$

$$d_\infty = \{1 + \exp[(-11.1 - V)/7.2]\}^{-1} \quad (14)$$

**TABLE 2 Structural and environmental parameters of the model**

| Parameter | Definition | Value |
|---|---|---|
| $r_{nucleus}$ | Radius to the surface of nucleus | 5.7934 $\mu$m |
| $r_{SR}$ | Radius to the surface of SR | 6 $\mu$m |
| $r_{SL}$ | Radius of the cell | 10.5 $\mu$m |
| $V_{SRrelease}$ | Velocity of $SR_{release}$ compartment | 0.009030 pl |
| $V_{SRuptake}$ | Velocity of $SR_{uptake}$ compartment | 0.08127 pl |
| $V_{cyto}$ | Velocity of the cytosol | 3.94 pl |
| $A_{cap}$ | Capacitive membrane area | $1.38544 \times 10^{-5}$ $cm^2$ |
| $F$ | Faradays constant | 96.5 C/mmol |
| $T$ | Temperature | 32°C = 305 K |
| $R$ | Ideal gas constant | 8.314 J / (mol K) |
| $C_m$ | Specific membrane capacitance | 1.0 $\mu$F/$cm^2$ |
| $[Ca^{2+}]_o$ | Extracellular $Ca^{2+}$ concentration | 1796 $\mu$M |
| $[Na^+]_o$ | Extracellular $Na^+$ concentration | 154578 $\mu$M |
| $[K^+]_o$ | Extracellular $K^+$ concentration | 5366 $\mu$M |

**TABLE 3 Parameters of the SL membrane currents**

| Parameter | Definition | Value |
|---|---|---|
| $G_{CaL}$ | Maximum $I_{CaL}$ conductance | $6.3 \times 10^{-5}$ $dm^3$ / (F ms) |
| $G_{CaT}$ | Maximum $I_{CaT}$ conductance | 0.2 mS/$\mu$F |
| $k_{NCX}$ | Scaling factor $I_{NCX}$ | $2.268 \times 10^{-16}$ pA / (pF $(\mu M)^4$) |
| $d_{NCX}$ | Denominator constant for $I_{NCX}$ | $10^{-16}$ $(\mu M)^{-4}$ |
| $\gamma$ | Energy barrier parameter for $I_{NCX}$ | 0.5 |
| $G_{Cab}$ | $I_{Cab}$ conductance | 0.0008 mS/$\mu$F |
| $G_{Nab}$ | $I_{Nab}$ conductance | 0.0026 mS/$\mu$F |
| $I_{NaK}^{max}$ | Maximum NaK-ATPase current | 2.7 pA/pF |
| $K_{m,Nai}$ | $Na^+$ half saturation constant for $I_{NaK}$ | 18600 $\mu$M |
| $n_{NaK}$ | Hill coefficient for $Na^+$ in $I_{NaK}$ | 3.2 |
| $K_{m,Ko}$ | $K^+$ half saturation constant for $I_{NaK}$ | 1500 $\mu$M |
| $G_{Na}$ | Maximum $I_{Na}$ conductance | 35 mS/$\mu$F |
| $G_f$ | Maximum $I_f$ conductance | 0.021 mS/$\mu$F |
| $G_{to}$ | Maximum $I_{to}$ conductance | 0.1 mS/$\mu$F |
| $G_{Ks}$ | Maximum $I_{Ks}$ conductance | 0.05 mS/$\mu$F |
| $G_{Kr}$ | Maximum $I_{Kr}$ conductance | 0.06 mS/$\mu$F |
| $k_f$ | Rate constant for $I_{Kr}$ | 0.023761 $ms^{-1}$ |
| $k_b$ | Rate constant for $I_{Kr}$ | 0.036778 $ms^{-1}$ |

$$\alpha_d = 1.4 \times \{1 + \exp[(-35 - V)/13]\}^{-1} + 0.25 \quad (15)$$

$$\beta_d = 1.4 \times \{1 + \exp[(V + 5)/5]\}^{-1} \quad (16)$$

$$\gamma_d = \{1 + \exp[(50 - V)/20]\}^{-1} \quad (17)$$

$$\tau_d = \alpha_d\beta_d + \gamma_d \quad (18)$$

$$f_\infty = \{1 + \exp[(23.3 + V)/5.4]\}^{-1} \quad (19)$$

$$\tau_f = 1125\exp[-(V + 27)^2/240] + 165 \times \{1 + \exp[(25 - V)/10]\}^{-1} + 120 \quad (20)$$

$$\alpha_{fCa} = \left[1 + \left([Ca^{2+}]_{subSL}/0.4875\right)^8\right]^{-1} \quad (21)$$

$$\beta_{fCa} = 0.1 \times \left\{1 + \exp\left[\left([Ca^{2+}]_{subSL} - 0.5\right)/0.1\right]\right\}^{-1} \quad (22)$$

$$\gamma_{fCa} = 0.2 \times \left\{1 + \exp\left[\left([Ca^{2+}]_{subSL} - 0.75\right)/0.8\right]\right\}^{-1} \quad (23)$$

**TABLE 4 Sarcoplasmic reticulum parameters**

| Parameter | Definition | Value |
|---|---|---|
| $k_{RyR}$ | Scaling factor for $J_{RyR}$ | 0.01 $ms^{-1}$ |
| $k_{open}$ | Rate constant for RyR opening | 1 $ms^{-1}$ |
| $k_{close}$ | Rate constant for RyR closing | 0.16 $ms^{-1}$ |
| $V_{max}$ | Maximum SERCA flux | 0.9996 $\mu$M/ms |
| $K_{mf}$ | Half-saturation for forward SERCA | 0.5 $\mu$M |
| $K_{mr}$ | Half-saturation for reverse SERCA | $7000 \times K_{mf} = 3500$ $\mu$M |
| $H$ | Hill coefficient for SERCA | 2 |
| $k_{leak}$ | SR leak rate constant | $5 \times 10^{-6}$ $ms^{-1}$ |
| $\tau_{tr}$ | Time constant for $J_{tr}$ | 200 ms |
| $[CSQN]_{tot}$ | Total calsequestrin concentration | 24750 $\mu$M |
| $K_{mCSQN}$ | Half-saturation for calsequestrin | 800 $\mu$M |

**TABLE 5 Cytosol parameters**

| Parameter | Definition | Value |
|---|---|---|
| $\Delta r$ | Length of spatial discretization of cytosol | 0.1 $\mu$m |
| $[TRPN]_{tot}$ | Total troponin concentration | 35 $\mu$M |
| $K_{mTRPN}$ | Half-saturation for troponin | 0.5 $\mu$M |
| $[CMDN]_{tot}$ | Total calmodulin concentration | 50 $\mu$M |
| $K_{mCMDN}$ | Half-saturation for calmodulin | 2.38 $\mu$M |
| $D_{Ca}$ | Diffusion coefficient for $Ca^{2+}$ | 7 $\mu m^2$/ms |
| $[EGTA]_{tot}$ | Total EGTA concentration | 1000 $\mu$M |
| $k_{EGTAon}$ | $Ca^{2+}$ on rate constant for EGTA | $1.5 \times 10^{-3}$ ($\mu$M ms)$^{-1}$ |
| $k_{EGTAoff}$ | $Ca^{2+}$ off rate constant for EGTA | $0.3 \times 10^{-3}$ ms$^{-1}$ |

$$f_{Ca\infty} = \left(\alpha_{fCa} + \beta_{fCa} + \gamma_{fCa} + 0.23\right)/1.46 \quad (24)$$

$$\tau_{fCa} = 10 \text{ ms} \quad (25)$$

$$\frac{dd}{dt} = \frac{d_\infty - d}{\tau_d} \quad (26)$$

$$\frac{df}{dt} = \frac{f_\infty - f}{\tau_f} \quad (27)$$

$$\frac{df_{Ca}}{dt} = k\frac{f_{Ca\infty} - f_{Ca}}{\tau_{fCa}}, \quad (28)$$

$$k = \begin{cases} 0 & \text{if } f_{Ca\infty} > f_{Ca} \text{ and } V > -60 \text{ mV} \\ 1 & \text{otherwise} \end{cases}$$

*T-type $Ca^{2+}$ current*

$$I_{CaT} = G_{CaT} bg(V - E_{Ca} + 106.5) \quad (29)$$

$$b_\infty = \{1 + \exp[-(V + 37.49098)/5.40634]\}^{-1} \quad (30)$$

$$\tau_b = 0.6 + 5.4 \times \{1 + \exp[0.03(V + 100)]\}^{-1} \quad (31)$$

$$g_\infty = \{1 + \exp[(V + 66)/6]\}^{-1} \quad (32)$$

$$\tau_g = 1 + 40 \times \{1 + \exp[0.08(V + 65)]\}^{-1} \quad (33)$$

$$\frac{db}{dt} = \frac{b_\infty - b}{\tau_b} \quad (34)$$

$$\frac{dg}{dt} = \frac{g_\infty - g}{\tau_g} \quad (35)$$

*$Na^+/Ca^{2+}$ exchanger*

$$I_{NCX} = k_{NCX}\frac{\left[Na^+\right]_i^3\left[Ca^{2+}\right]_o \exp(0.03743\gamma V) - \left[Na^+\right]_o^3\left[Ca^{2+}\right]_{subSL} \exp[0.03743(\gamma - 1)V]}{1 + d_{NCX}\left(\left[Na^+\right]_o^3\left[Ca^{2+}\right]_{subSL} + \left[Na^+\right]_i^3\left[Ca^{2+}\right]_o\right)} \quad (36)$$

*Background $Ca^{2+}$ and $Na^+$ currents*

$$I_{Cab} = G_{Cab}(V - E_{Ca}) \quad (37)$$

$$I_{Nab} = G_{Nab}(V - E_{Na}) \quad (38)$$

*$Na^+/K^+$ ATPase*

$$I_{NaK} = I_{NaK}^{max} f_{NaK} \times \left[1 + \left(K_{m,Nai}/\left[Na^+\right]_i\right)^{n_{NaK}}\right]^{-1} \times \left[1 + \left(K_{m,Ko}/\left[K^+\right]_o\right)\right]^{-1} \quad (39)$$

$$f_{NaK} = [1 + 0.1245 \exp(-0.1VF/RT) + 0.0365\sigma \exp(-VF/RT)]^{-1} \quad (40)$$

$$\sigma = 1/7 \times \left[\exp\left(\left[Na^+\right]_o/67300\right) - 1\right] \quad (41)$$

*Fast $Na^+$ current*

$$I_{Na} = G_{Na} m^3 hj(V - E_{Na}) \quad (42)$$

$$m_\infty = \{1 + \exp[(45 + V)/-6.5]\}^{-1} \quad (43)$$

$$j_\infty = h_\infty = \{1 + \exp[(76.1 + V)/6.07]\}^{-1} \quad (44)$$

$$\tau_m = 1.36 \times \left\{\frac{0.32(V + 47.13)}{1 - \exp[-0.1(V + 47.13)]} + 0.08 \exp(-V/11)\right\}^{-1} \quad (45)$$

if $V \geq -40$ mV,

$$\tau_h = 0.4537\{1 + \exp[(V + 10.66)/-11.1]\} \quad (46)$$

$$\tau_j = 11.63 \times \{1 + \exp[-0.1(V + 32)]\} \times \left\{\exp[-2.535 \times 10^{-7}V]\right\}^{-1} \quad (47)$$

and if $V < -40$ mV

$$\tau_h = 3.49 \times \left\{0.135 \exp[(V + 80)/-6.8] + 3.56 \exp(0.079V) + 3.1 \times 10^5 \exp(0.35V)\right\}^{-1} \quad (48)$$

$$\tau_j = 3.49 \times \left\{ \frac{V + 37.78}{1 + \exp[0.311(V + 79.23)]} [-127140 \exp(0.2444V) - 3.474 \times 10^{-5} \exp(-0.04391V)] + \frac{0.1212 \exp(-0.01052V)}{1 + \exp[-0.1378(V + 40.14)]} \right\}^{-1} \quad (49)$$

$$\frac{dm}{dt} = \frac{m_\infty - m}{\tau_m} \quad (50)$$

$$\frac{dh}{dt} = \frac{h_\infty - h}{\tau_h} \quad (51)$$

$$\frac{dj}{dt} = \frac{j_\infty - j}{\tau_j} \quad (52)$$

*Hyperpolarization activated current*

$$I_{f\mathrm{Na}} = G_f y[0.2(V - E_{\mathrm{Na}})] \quad (53)$$

$$I_{f\mathrm{K}} = G_f y[0.8(V - E_{\mathrm{K}})] \quad (54)$$

$$I_f = I_{f\mathrm{Na}} + I_{f\mathrm{K}} \quad (55)$$

$$y_\infty = \{1 + \exp[(V + 78.65)/6.33]\}^{-1} \quad (56)$$

$$\tau_y = 1000 \times \{0.11885 \exp[(V + 75)/28.37] + 0.56236 \exp[(V + 75)/-14.19]\}^{-1} \quad (57)$$

$$\frac{dy}{dt} = \frac{y_\infty - y}{\tau_y} \quad (58)$$

*Time-independent $K^+$ current*

$$I_{\mathrm{K1}} = 0.0515 \frac{[\mathrm{K}^+]_\mathrm{o}}{[\mathrm{K}^+]_\mathrm{o} + 210} \frac{V - E_{\mathrm{K}} - 6.1373}{0.1653 + e^{0.0319(V - E_{\mathrm{K}} - 6.1373)}} \quad (59)$$

*Transient outward $K^+$ current*

$$I_{\mathrm{to}} = G_{\mathrm{to}} r(0.706s + 0.294 s_{\mathrm{slow}})(V - E_{\mathrm{K}}) \quad (60)$$

$$r_\infty = \{1 + \exp[(V - 3.55716)/-14.61299]\}^{-1} \quad (61)$$

$$s_{\mathrm{slow}\infty} = s_\infty = \{1 + \exp[(V + 31.97156)/4.64291]\}^{-1} \quad (62)$$

$$\tau_r = 1000 \times \{45.16 \exp[0.03577(V + 50)] + 98.9 \exp[-0.1(V + 38)]\}^{-1} \quad (63)$$

$$\tau_s = 1000 \times \{0.35 \exp[-((V + 70)/15)^2] + 0.035\} - 26.9 \quad (64)$$

$$\tau_{s,\mathrm{slow}} = 1000 \times \{3.7 \exp[-((V + 70)/30)^2] + 0.035\} + 37.4 \quad (65)$$

$$\frac{dr}{dt} = \frac{r_\infty - r}{\tau_r} \quad (66)$$

$$\frac{ds}{dt} = \frac{s_\infty - s}{\tau_s} \quad (67)$$

$$\frac{ds_{\mathrm{slow}}}{dt} = \frac{s_{\mathrm{slow}\infty} - s_{\mathrm{slow}}}{\tau_{s,\mathrm{slow}}} \quad (68)$$

*Slow delayed rectifier $K^+$ current*

$$I_{\mathrm{Ks}} = G_{\mathrm{Ks}} n_{\mathrm{Ks}}^2 (V - E_{\mathrm{K}}) \quad (69)$$

$$\alpha_n = 0.00000481333(V + 26.5) \times \{1 - \exp[-0.128(V + 26.5)]\}^{-1} \quad (70)$$

$$\beta_n = 0.0000953333 \exp[-0.038(V + 26.5)] \quad (71)$$

$$n_{\mathrm{Ks}\infty} = \alpha_n/(\alpha_n + \beta_n) \quad (72)$$

$$\tau_{n\mathrm{Ks}} = 750 \text{ ms} \quad (73)$$

$$\frac{dn_{\mathrm{Ks}}}{dt} = \frac{n_{Ks\infty} - n_{\mathrm{Ks}}}{\tau_{n\mathrm{Ks}}} \quad (74)$$

*Rapid delayed rectifier $K^+$ current*

$$I_{\mathrm{Kr}} = O_{\mathrm{K}} G_{\mathrm{Kr}} \left[ V - \frac{RT}{F} \ln \left( \frac{0.98[\mathrm{K}^+]_\mathrm{o} + 0.02[\mathrm{Na}^+]_\mathrm{o}}{0.98[\mathrm{K}^+]_\mathrm{i} + 0.02[\mathrm{Na}^+]_\mathrm{i}} \right) \right] \quad (75)$$

$$\alpha_{a0} = 0.022348 \exp(0.01176V) \quad (76)$$

$$\beta_{a0} = 0.047002 \exp(-0.0631V) \quad (77)$$

$$\alpha_{a1} = 0.013733 \exp(0.038198V) \quad (78)$$

$$\beta_{a1} = 0.0000689\exp(-0.04178V) \quad (79)$$

$$\alpha_{\rm i} = 0.090821\exp(0.023391V) \quad (80)$$

$$\beta_{\rm i} = 0.006497\exp(-0.03268V) \quad (81)$$

$$C_{\rm K0} = 1-(C_{\rm K1}+C_{\rm K2}+O_{\rm K}+I_{\rm K}) \quad (82)$$

$$\frac{dC_{\rm K1}}{dt} = \alpha_{a0}C_{\rm K0}-\beta_a C_{\rm K1}+k_b C_{\rm K2}-k_f C_{\rm K1} \quad (83)$$

$$\frac{dC_{\rm K2}}{dt} = kC_{\rm K1}-k_b C_{\rm K2}+\beta_{a1}O_{\rm K}-\alpha_{a1}C_{\rm K2} \quad (84)$$

$$\frac{dO_{\rm K}}{dt} = \alpha_{a1}C_{\rm K2}-\beta_{a1}O_{\rm K}+\beta_{\rm i}I_{\rm K}-\alpha_{\rm i}O_{\rm K} \quad (85)$$

$$\frac{dI_{\rm K}}{dt} = \alpha_{\rm i}O_{\rm K}-\beta_{\rm i}I_{\rm K} \quad (86)$$

$$\frac{dV}{dt} = -\big(I_{\rm CaL}+I_{\rm CaT}+I_{\rm NCX}+I_{\rm Cab}+I_{\rm Nab}+I_{\rm NaK}+I_{\rm Na}+I_{\rm f}+I_{\rm K1}+I_{\rm to}+I_{\rm Ks}+I_{\rm Kr}+I_{\rm stim}\big) \quad (87)$$

## Sarcoplasmic reticulum

### *Ryanodine receptors*

$$J_{\rm RyR} = k_{\rm RyR}P_{\rm open}\big([{\rm Ca}^{2+}]_{\rm SRrelease}-[{\rm Ca}^{2+}]_{\rm subSR}\big) \quad (88)$$

$$J_{\rm RyR\text{-}Caffeine} = 5.5\times10^{-4}{\rm ms}\times([{\rm Ca}^{2+}]_{\rm SRrelease}-[{\rm Ca}^{2+}]_{\rm subSR}) \quad (92)$$

$$K_{\rm m,RyR} = 3.51\times\big\{1+\exp\big[\big([{\rm Ca}^{2+}]_{\rm SRrelease}-530\big)/200\big]\big\}^{-1}+0.25 \quad (90)$$

$$P_{\rm closed} = 1-P_{\rm open} \quad (91)$$

$$\frac{dP_{\rm open}}{dt} = P_{\rm closed}k_{\rm open}\times\Big[1+\big(K_{\rm m,RyR}/[{\rm Ca}^{2+}]_{\rm subSR}\big)^4\Big]^{-1}-k_{\rm close}P_{\rm open} \quad (92)$$

### *SERCA*

$$J_{\rm SERCA} = \frac{V_{\rm max}\big([{\rm Ca}^{2+}]_{\rm subSR}/K_{\rm mf}\big)^H-V_{\rm max}\Big([{\rm Ca}^{2+}]_{\rm SRuptake}/K_{\rm mr}\Big)^H}{1+\big([{\rm Ca}^{2+}]_{\rm subSR}/K_{\rm mf}\big)^H+\Big([{\rm Ca}^{2+}]_{\rm SRuptake}/K_{\rm mr}\Big)^H} \quad (93)$$

### *Leak flux*

$$J_{\rm leak} = k_{\rm leak}\Big([{\rm Ca}^{2+}]_{\rm SRuptake}-[{\rm Ca}^{2+}]_{\rm subSR}\Big) \quad (94)$$

### *$Ca^{2+}$ diffusion between SRuptake and SRrelease*

$$J_{\rm tr} = \Big([{\rm Ca}^{2+}]_{\rm SRuptake}-[{\rm Ca}^{2+}]_{\rm SRrelease}\Big)/\tau_{\rm tr} \quad (95)$$

### *$Ca^{2+}$ concentration in SR*

$$\beta_{\rm SRrelease} = \Big[1+[{\rm CSQN}]_{\rm tot}K_{\rm mCSQN}/\big([{\rm Ca}^{2+}]_{\rm SRrelease}+K_{\rm mCSQN}\big)^2\Big]^{-1} \quad (96)$$

$$\frac{d[{\rm Ca}^{2+}]_{\rm SRuptake}}{dt} = (J_{\rm SERCA}-J_{\rm leak}-J_{\rm tr})/V_{\rm SRuptake} \quad (97)$$

$$\frac{d[{\rm Ca}^{2+}]_{\rm SRrelease}}{dt} = \beta_{\rm SRrelease}\big(-J_{\rm RyR}+J_{\rm tr}\big)/V_{\rm SRrelease} \quad (98)$$

## Cytosol

### *$Na^{+}$ concentration*

$$\frac{d[{\rm Na}^+]_{\rm i}}{dt} = -\big(I_{\rm fNa}+I_{\rm Nab}+I_{\rm Na}+3I_{\rm NCX}+3I_{\rm NaK}\big)\frac{A_{\rm cap}C_{\rm m}}{FV_{\rm cyto}\times10^{-6}\mu{\rm l/pl}} \quad (99)$$

### *$K^{+}$ concentration*

$$\frac{d[{\rm K}^+]_{\rm i}}{dt} = -\big(I_{\rm fK}+I_{\rm to}+I_{\rm K1}+I_{\rm Ks}+I_{\rm Kr}-2I_{\rm NaK}+I_{\rm stim}\big)\frac{A_{\rm cap}C_{\rm m}}{FV_{\rm cyto}\times10^{-6}\mu{\rm l/pl}} \quad (100)$$

### *$Ca^{2+}$ concentration*

In the following equations, $c = [{\rm Ca}^{2+}]_{\rm i}$

$$\beta_i(c) = \left[1 + [\mathrm{TRPN}]_{tot} K_{mTRPN}/(c + K_{mTRPN})^2 + [\mathrm{CMDN}]_{tot} K_{mCMDN}/(c + K_{mCMDN})^2\right]^{-1} \quad (101)$$

The general equation for $Ca^{2+}$ diffusion in spherical coordinates with radial symmetry is

$$\frac{\partial c(r,t)}{\partial t} = \beta_i(c(r,t))\left[D_{Ca}\frac{\partial^2 c(r,t)}{\partial r^2} + \frac{2D_{Ca}}{r}\frac{\partial c(r,t)}{\partial r} + J_{Ca}(r,t)\right] \quad (102)$$

which is reduced to a system of ODEs for the simulation by approximating the radial derivatives with step lengths of $\Delta r$. I.e. the cytosol is divided into spherical cores with a thickness of $\Delta r$. To calculate the concentrations at the centers of these spherical cores we define a vector

$$j = [\, r_{SR} + 0.5\Delta r \quad r_{SR} + 0.5\Delta r + \Delta r \quad r_{SR} + 0.5\Delta r + 2\Delta r \ldots r_{SL} - 0.5\Delta r]/\Delta r \quad (103)$$

Thus, $j_n \Delta r$ is the spatial coordinate for concentration $c_n$. The system of ODEs for the $Ca^{2+}$ diffusion with the reflecting boundary conditions at $r_{SL}$ and $r_{SL}$ and with SR and SL $Ca^{2+}$ fluxes is

for $n = 1$

$$\frac{dc_n}{dt} = \beta_i(c_n)\left\{\frac{D_{Ca}}{j_n(\Delta r)^2}[(1 + j_n)c_{n+1} - 2j_n c_n + (j_n - 1)c_n] + \frac{J_{CaSR}}{V_{subSR}}\right\} \quad (104)$$

for $n = 2,3,4,\ldots, a - 1$

$$\frac{dc_n}{dt} = \beta_i(c_n)\frac{D_{Ca}}{j_n(\Delta r)^2}[(1 + j_n)c_{n+1} - 2j_n c_n + (j_n - 1)c_{n-1}] \quad (105)$$

for $n = a$

$$\frac{dc_n}{dt} = \beta_i(c_n)\left\{\frac{D_{Ca}}{j_n(\Delta r)^2}[(1 + j_n)c_n - 2j_n c_n + (j_n - 1)c_{n-1}] + \frac{J_{CaSL}}{V_{subSL}}\right\}, \quad (106)$$

where $a$ is the number of components in the vector **j** and

$$J_{CaSR} = J_{RyR} - J_{SERCA} + J_{leak} \quad (107)$$

$$J_{CaSL} = (2I_{NCX} - I_{CaL} - I_{CaT} - I_{Cab})\frac{A_{cap}C_m}{2F \times 10^{-6}\mu\mathrm{l/pl}} \quad (108)$$

$$V_{subSR} = \left[\frac{4}{3}\pi(r_{SR} + \Delta r)^3 - \frac{4}{3}\pi r_{SR}\right] \times 10^{-3}\ \mathrm{pl/fl} \quad (109)$$

$$V_{subSL} = \left[\frac{4}{3}\pi r_{SL} - \frac{4}{3}\pi(r_{SL} - \Delta r)^3\right] \times 10^{-3}\mathrm{pl/fl}. \quad (110)$$

In some simulations, the flux to EGTA buffer ($-J_{EGTAn}$) was added to Eqs. 104–106 in the place of $J_{Ca}(r,t)$ in Eq. 102, and additional differential variables for the amount of bound $Ca^{2+}$ ([EGTACa]) were calculated for $n = 1,2,\ldots a$

$$J_{EGTAn} = k_{EGTAon}c_n([\mathrm{EGTA}]_{tot} - [\mathrm{EGTACa}]_n) - k_{EGTAoff}[\mathrm{EGTACa}]_n \quad (111)$$

$$\frac{d[\mathrm{EGTACa}]_n}{dt} = J_{EGTAn}. \quad (112)$$

We thank A. Rautio, J. Ronkainen and E. Kouvalainen for technical assistance and J. Takalo for valuable discussions on the model development.

This study was supported by the Finnish Heart Research Foundation, Academy of Finland, Orion-Farmos Research Foundation, Instrumentarium Science Foundation, Aarne Koskelo Foundation, and Sigrid Juselius Foundation.

## REFERENCES

1. Bers, D. M. 2001. Excitation-contraction coupling and cardiac contractile force. Kluwer, Dordrecht, London.
2. Bondarenko, V. E., G. P. Szigeti, G. C. L. Bett, S. J. Kim, and R. L. Rasmusson. 2004. Computer model of action potential of mouse ventricular myocytes. *Am. J. Physiol. Heart Circ. Physiol.* 287:H1378–H1403.
3. Tavi, P., C. L. Han, and M. Weckstrom. 1998. Mechanisms of stretch-induced changes in $[Ca^{2+}]_i$ in rat atrial myocytes: role of increased troponin C affinity and stretch-activated ion channels. *Circ. Res.* 83:1165–1177.
4. Dokos, S., B. Celler, and N. Lovell. 1996. Ion currents underlying sino-atrial node pacemaker activity: a new single cell mathematical model. *J. Theor. Biol.* 181:245–272.
5. ten Tusscher, K. H. W. J., D. Noble, P. J. Noble, and A. V. Panfilov. 2004. A model for human ventricular tissue. *Am. J. Physiol. Heart Circ. Physiol.* 286:H1573–H1589.
6. Pandit, S. V., R. B. Clark, W. R. Giles, and S. S. Demir. 2001. A mathematical model of action potential heterogeneity in adult rat left ventricular myocytes. *Biophys. J.* 81:3029–3051.
7. Luo, C. H., and Y. Rudy. 1994. A dynamic model of the cardiac ventricular action potential. 1. Simulations of ionic currents and concentration changes. *Circ. Res.* 74:1071–1096.
8. Shannon, T. R., F. Wang, J. Puglisi, C. Weber, and D. M. Bers. 2004. A mathematical treatment of integrated Ca dynamics within the ventricular myocyte. *Biophys. J.* 87:3351–3371.
9. Wang, L. J., and E. A. Sobie. 2008. Mathematical model of the neonatal mouse ventricular action potential. *Am. J. Physiol. Heart Circ. Physiol.* 294:H2565–H2575.
10. Korhonen, T., R. Rapila, and P. Tavi. 2008. Mathematical model of mouse embryonic cardiomyocyte excitation-contraction coupling. *J. Gen. Physiol.* 132:407–419.
11. Ronkainen, V. P., J. J. Ronkainen, S. L. Hannninen, H. Leskinen, J. L. Ruas, et al. 2007. Hypoxia inducible factor regulates the cardiac expression and secretion of apelin. *FASEB J.* 21:1821–1830.
12. Ronkainen, J. J., O. Vuolteenaho, and P. Tavi. 2007. Calcium-calmodulin kinase II is the common factor in calcium-dependent cardiac expression and secretion of A- and B-type natriuretic peptides. *Endocrinology.* 148:2815–2820.

13. Seki, S., M. Nagashima, Y. Yamada, M. Tsutsuura, T. Kobayashi, et al. 2003. Fetal and postnatal development of $Ca^{2+}$ transients and $Ca^{2+}$ sparks in rat cardiomyocytes. *Cardiovasc. Res.* 58:535–548.

14. Avila, G., I. M. Medina, E. Jimenez, G. Elizondo, and C. I. Aguilar. 2007. Transforming growth factor-$\beta$ 1 decreases cardiac muscle L-type $Ca^{2+}$ current and charge movement by acting on the Ca(v)1.2 mRNA. *Am. J. Physiol. Heart Circ. Physiol.* 292:H622–H631.

15. Delcarpio, J. B., W. C. Claycomb, and R. L. Moses. 1989. Ultrastructural morphometric analysis of cultured neonatal and adult-rat ventricular cardiac-muscle cells. *Am. J. Anat.* 186:335–345.

16. Seth, M., C. Surnbilla, S. P. Mullen, D. Lewis, M. G. Klein, et al. 2004. Sarco(endo)plasmic reticulurn $Ca^{2+}$ ATPase (SERCA) gene silencing and remodeling of the $Ca^{2+}$ signaling mechanism in cardiac myocytes. *Proc. Natl. Acad. Sci. USA.* 101:16683–16688.

17. Periasamy, M., and A. Kalyanasundaram. 2007. SERCA pump isoforms: their role in calcium transport and disease. *Muscle Nerve.* 35:430–442.

18. Michailova, A., F. DelPrincipe, M. Egger, and E. Niggli. 2002. Spatiotemporal features of $Ca^{2+}$ buffering and diffusion in atrial cardiac myocytes with inhibited sarcoplasmic reticulum. *Biophys. J.* 83:3134–3151.

19. Haddock, P. S., W. A. Coetzee, E. Cho, L. Porter, H. Katoh, et al. 1999. Subcellular $[Ca^{2+}]_i$ gradients during excitation-contraction coupling in newborn rabbit ventricular myocytes. *Circ. Res.* 85:415–427.

20. Guo, J., H. Massaeli, W. Li, J. M. Xu, T. Luo, et al. 2007. Identification of I-Kr and its trafficking disruption induced by probucol in cultured neonatal rat cardiomyocytes. *J. Pharmacol. Exp. Ther.* 321:911–920.

21. Pignier, C., and D. Potreau. 2000. Characterization of nifedipine-resistant calcium current in neonatal rat ventricular cardiomyocytes. *Am. J. Physiol. Heart Circ. Physiol.* 279:H2259–H2268.

22. Xiao, Y. F., A. M. Gomez, J. P. Morgan, W. J. Lederer, and A. Leaf. 1997. Suppression of voltage-gated L-type $Ca^{2+}$ currents by polyunsaturated fatty acids in adult and neonatal rat ventricular myocytes. *Proc. Natl. Acad. Sci. USA.* 94:4182–4187.

23. Shi, W. M., R. Wymore, H. G. Yu, J. Y. Wu, R. T. Wymore, et al. 1999. Distribution and prevalence of hyperpolarization-activated cation channel (HCN) mRNA expression in cardiac tissues. *Circ. Res.* 85: E1–E6.

24. Robinson, R. B., H. G. Yu, F. Chang, and I. S. Cohen. 1997. Developmental change in the voltage-dependence of the pacemaker current, $i_f$, in rat ventricle cells. *Pflug. Arch.* 433:533–535.

25. Wahler, G. M. 1992. Developmental increases in the inwardly rectifying potassium current of rat ventricular myocytes. *Am. J. Physiol.* 262: C1266–C1272.

26. Walsh, K. B., J. K. Sweet, G. E. Parks, and K. J. Long. 2001. Modulation of outward potassium currents in aligned cultures of neonatal rat ventricular myocytes during phorbol ester-induced hypertrophy. *J. Mol. Cell. Cardiol.* 33:1233–1247.

27. Kamiya, K., W. N. Guo, K. Yasui, and J. Toyama. 1999. Hypoxia inhibits the changes in action potentials and ion channels during primary culture of neonatal rat ventricular myocytes. *J. Mol. Cell. Cardiol.* 31:1591–1598.

28. Gaughan, J. P., C. A. Hefner, and S. R. Houser. 1998. Electrophysiological properties of neonatal rat ventricular myocytes with $\alpha_1$-adrenergic-induced hypertrophy. *Am. J. Physiol.* 275:H577–H590.

29. Munoz, V., K. R. Grzeda, T. Desplantez, S. V. Pandit, S. Mironov, et al. 2007. Adenoviral expression of I-Ks contributes to wavebreak and fibrillatory conduction in neonatal rat ventricular cardiomyocyte monolayers. *Circ. Res.* 101:475–483.

30. Wang, S. M., S. G. Liu, M. J. Morales, H. C. Strauss, and R. L. Rasmusson. 1997. A quantitative analysis of the activation and inactivation kinetics of HERG expressed in *Xenopus* oocytes. *J. Physiol.* 502:45–60.

31. Nuss, H. B., and E. Marban. 1994. Electrophysiological properties of neonatal mouse cardiac myocytes in primary culture. *J. Physiol.* 479:265–279.

32. Shannon, T. R., K. S. Ginsburg, and D. M. Bers. 2000. Reverse mode of the sarcoplasmic reticulum calcium pump and load-dependent cytosolic calcium decline in voltage-clamped cardiac ventricular myocytes. *Biophys. J.* 78:322–333.

33. Ioshii, S. O., K. Imanakayoshida, and T. Yoshida. 1994. Organization of calsequestrin-positive sarcoplasmic reticulum in rat cardiomyocytes in culture. *J. Cell. Physiol.* 158:87–96.

34. Sobie, E. A., K. W. Dilly, J. D. Cruz, W. J. Lederer, and M. S. Jafri. 2002. Termination of cardiac $Ca^{2+}$ sparks: an investigative mathematical model of calcium-induced calcium release. *Biophys. J.* 83:59–78.

35. Dawson, S. P., J. Keizer, and J. E. Pearson. 1999. Fire-diffuse-fire model of dynamics of intracellular calcium waves. *Proc. Natl. Acad. Sci. USA.* 96:6060–6063.

36. Keener, J. P., and J. Sneyd. 1998. Mathematical Physiology. Springer, New York.

37. Bassani, R. A., T. R. Shannon, and D. M. Bers. 1998. Passive $Ca^{2+}$ binding in ventricular myocardium of neonatal and adult rats. *Cell Calcium.* 23:433–442.

38. Creazzo, T. L., J. Burch, and R. E. Godt. 2004. Calcium buffering and excitation-contraction coupling in developing avian myocardium. *Biophys. J.* 86:966–977.

39. Anversa, P., A. V. Loud, F. Giacomelli, and J. Wiener. 1978. Absolute morphometric study of myocardial hypertrophy in experimental hypertension. II. Ultrastructure of myocytes and interstitium. *Lab. Invest.* 38:597–609.

40. Smith, P. D., G. W. Liesegang, R. L. Berger, G. Czerlinski, and R. J. Podolsky. 1984. A stopped-flow investigation of calcium ion binding by ethylene glycol bis($\beta$-aminoethyl ether)-N,N'-tetraacetic acid. *Anal. Biochem.* 143:188–195.

41. Hund, T. J., J. P. Kucera, N. F. Otani, and Y. Rudy. 2001. Ionic charge conservation and long-term steady state in the Luo-Rudy dynamic cell model. *Biophys. J.* 81:3324–3331.

42. Voutilainen-Myllyla, S., P. Tavi, and M. Weckstrom. 2003. Chelerythrine and bisindolylmaleimide I prolong cardiac action potentials by protein kinase C-independent mechanism. *Eur. J. Pharmacol.* 466: 41–51.

43. Motlagh, D., K. J. Alden, B. Russell, and J. Garcia. 2002. Sodium current modulation by a tubulin/GTP coupled process in rat neonatal cardiac myocytes. *J. Physiol.* 540:93–103.

44. Hojo, Y., U. Ikeda, Y. Tsuruya, H. Ebata, M. Murata, et al. 1997. Thyroid hormone stimulates $Na^+$-$Ca^{2+}$ exchanger expression in rat cardiac myocytes. *J. Cardiovasc. Pharmacol.* 29:75–80.

45. Hayasaki-Kajiwara, Y., Y. Kitano, T. Iwasaki, T. Shimamura, N. Naya, et al. 1999. $Na^+$ influx via $Na^+/H^+$ exchange activates protein kinase C isozymes $\delta$ and $\varepsilon$ in cultured neonatal rat cardiac myocytes. *J. Mol. Cell. Cardiol.* 31:1559–1572.

46. Bers, D. M., D. M. Christensen, and T. X. Nguyen. 1988. Can Ca entry via Na-Ca exchange directly activate cardiac-muscle contraction. *J. Mol. Cell. Cardiol.* 20:405–414.

47. Guo, W. N., K. Kamiya, J. H. Cheng, and J. J. Toyama. 1996. Changes in action potentials and ion currents in long-term cultured neonatal rat ventricular cells. *Am. J. Physiol. Cell Physiol.* 40:C93–C102.

48. Pang, Y., D. L. Hunton, P. Bounelis, and R. B. Marchase. 2002. Hyperglycemia inhibits capacitative calcium entry and hypertrophy in neonatal cardiomyocytes. *Diabetes.* 51:3461–3467.

49. Lokuta, A., M. S. Kirby, S. T. Gaa, W. J. Lederer, and T. B. Rogers. 1994. Establishing primary cultures of neonatal rat ventricular myocytes for analysis over long periods. *J. Cardiovasc. Electrophysiol.* 5:50–62.

50. Kapiloff, M. S., N. Jackson, and N. Airhart. 2001. mAKAP and the ryanodine receptor are part of a multicomponent signaling complex on the cardiomyocyte nuclear envelope. *J. Cell Sci.* 114:3167–3176.

51. Sheehan, K. A., and L. A. Blatter. 2003. Regulation of junctional and non-junctional sarcoplasmic reticulum calcium release in excitation-contraction coupling in cat atrial myocytes. *J. Physiol.* 546:119–135.

52. Cussler, E. L. 1997. Diffusion mass transfer in fluid systems. Cambridge University Press, Cambridge, United Kingdom.

53. Kushmerick, M. J., and R. J. Podolsky. 1969. Ionic mobility in muscle cells. *Science.* 166:1297–1298.

54. Huser, J., S. L. Lipsius, and L. A. Blatter. 1996. Calcium gradients during excitation-contraction coupling in cat atrial myocytes. *J. Physiol.* 494:641–651.

55. Kirby, M. S., Y. Sagara, S. Gaa, G. Inesi, W. J. Lederer, et al. 1992. Thapsigargin inhibits contraction and $Ca^{2+}$ transient in cardiac cells by specific inhibition of the sarcoplasmic reticulum $Ca^{2+}$ pump. *J. Biol. Chem.* 267:12545–12551.

56. Prasad, A. M., H. Ma, C. Sumbilla, D. I. Lee, M. G. Klein, et al. 2007. Phenylephrine hypertrophy, $Ca^{2+}$-ATPase (SERCA2), and $Ca^{2+}$ signaling in neonatal rat cardiac myocytes. *Am. J. Physiol. Cell Physiol.* 292:C2269–C2275.

57. Barac, Y. D., N. Zeevi-Levin, G. Yaniv, I. Reiter, F. Milman, et al. 2005. The 1,4,5-inositol trisphosphate pathway is a key component in Fas-mediated hypertrophy in neonatal rat ventricular myocytes. *Cardiovasc. Res.* 68:75–86.

58. Bers, D. M., W. H. Barry, and S. Despa. 2003. Intracellular $Na^{+}$ regulation in cardiac myocytes. *Cardiovasc. Res.* 57:897–912.

59. Guo, W., H. Xu, and J. Nerbonne. 1999. Molecular basis of transient outward $K^{+}$ current diversity in mouse ventricular myocytes. *J. Physiol.* 521:587–599.

60. Pogwizd, S. M., K. Schlotthauer, L. Li, W. L. Yuan, and D. M. Bers. 2001. Arrhythmogenesis and contractile dysfunction in heart failure: roles of sodium-calcium exchange, inward rectifier potassium current, and residual $\beta$-adrenergic responsiveness. *Circ. Res.* 88:1159–1167.

61. Liu, D. W., and C. Antzelevitch. 1995. Characteristics of the delayed rectifier current ($I_{Kr}$ and $I_{Ks}$) in canine ventricular epicardial, midmyocardial, and endocardial myocytes: a weaker $I_{Ks}$ contributes to the longer action-potential of the M cell. *Circ. Res.* 76:351–365.

62. Taggart, P., P. M. I. Sutton, M. R. Boyett, M. Lab, and H. Swanton. 1996. Human ventricular action potential duration during short and long cycles: rapid modulation by ischemia. *Circulation.* 94:2526–2534.

63. Han, C. L., P. Tavi, and M. Weckstrom. 2002. Role of the $Na^{+}$-$Ca^{2+}$ exchanger as an alternative trigger of CICR in mammalian cardiac myocytes. *Biophys. J.* 82:1483–1496.

64. Bassani, J. W. M., M. Qi, A. M. Samarel, and D. M. Bers. 1994. Contractile arrest increases sarcoplasmic reticulum calcium uptake and SERCA2 gene expression in cultured neonatal rat heart cells. *Circ. Res.* 74:991–997.

65. McCall, E., K. S. Ginsburg, R. A. Bassani, T. R. Shannon, M. Qi, et al. 1998. Ca flux, contractility, and excitation-contraction coupling in hypertrophic rat ventricular myocytes. *Am. J. Physiol. Heart Circ. Physiol.* 43:H1348–H1360.

66. Delbridge, L. M. D., H. Satoh, W. Yuan, J. W. M. Bassani, M. Qi, et al. 1997. Cardiac myocyte volume, $Ca^{2+}$ fluxes, and sarcoplasmic reticulum loading in pressure-overload hypertrophy. *Am. J. Physiol.* 41: H2425–H2435.

67. Diaz, M. E., A. W. Trafford, S. C. O. Neill, and D. A. Eisner. 1997. A measurable reduction of SR Ca content follows spontaneous Ca release in rat ventricular myocytes. *Pflug Arch. Eur. J. Physiol.* 434:852–854.

68. Aydin, J., T. Korhonen, P. Tavi, D. G. Allen, H. Westerblad, et al. 2007. Activation of $Ca^{2+}$-dependent protein kinase II during repeated contractions in single muscle fibres from mouse is dependent on the frequency of sarcoplasmic reticulum $Ca^{2+}$ release. *Acta Physiologica.* 191:131–137.

69. Tavi, P., S. Pikkarainen, J. Ronkainen, P. Niemela, M. Ilves, et al. 2004. Pacing-induced calcineurin activation controls cardiac $Ca^{2+}$ signalling and gene expression. *J. Physiol.* 554:309–320.

70. Tavi, P., D. G. Allen, P. Niemela, O. Vuolteenaho, M. Weckstrom, et al. 2003. Calmodulin kinase modulates $Ca^{2+}$ release in mouse skeletal muscle. *J. Physiol.* 551:5–12.

71. Rapila, R., T. Korhonen, and P. Tavi. 2008. Excitation-contraction coupling of the mouse embryonic cardiomyocyte. *J. Gen. Physiol.* 132:397–405.

72. Mackenzie, L., H. L. Roderick, M. J. Berridge, S. J. Conway, and M. D. Bootman. 2004. The spatial pattern of atrial cardiomyocyte calcium signalling modulates contraction. *J. Cell Sci.* 117:6327–6337.